Cruces-Zabala, J., Ritter, O., Tietze, K., Weckmann, U., Schmitz, M. (2020): Magnetotelluric imaging of the Mérida Andes and surrounding areas in Venezuela. - Geophysical Journal International, 222, 3, 1570-1589.

https://doi.org/10.1093/gji/ggaa266

Geophysical Journal International

Geophys. J. Int. (2020) **222,** 1570–1589
Advance Access publication 2020 June 01
GJI Geodynamics and Tectonics

doi: 10.1093/gji/ggaa266

Magnetotelluric imaging of the Mérida Andes and surrounding areas in Venezuela

J. Cruces-Zabala,[1,2,3] O. Ritter,[1,3] U. Weckmann,[1,4] K. Tietze[1,3] and M. Schmitz[2]

[1] *Near-surface Geophysics , GFZ German Research Center for Geosciences, 14473, Potsdam, Germany. E-mail: jcruces@gfz-potsdam.de*
[2] *Departament of geophysics, FUNVISIS Venezuelan Foundation for Seismological Research, 1070, Caracas, Venezuela,*
[3] *Geophysics Section, Freie Universität Berlin, 12249, Berlin, Germany*
[4] *Institute of Earth and Environmental Science, University of Potsdam, 14476 , Potsdam, Germany*

Accepted 2020 May 28. Received 2020 May 15; in original form 2019 November 25

SUMMARY

The Caribbean and South American tectonic plates bound the north-eastwards expulsion of the North Andean Block in western Venezuela. This complex geodynamic setting resulted in the formation of major strike-slip fault systems and sizeable mountain chains. The 100-km-wide Mérida Andes extend from the Colombian/Venezuelan border to the Caribbean coast. To the north and south, the Mérida Andes are bound by hydrocarbon-rich sedimentary basins. Knowledge of lithospheric structures, related to the formation of the Mérida Andes, is limited though, due to a lack of deep geophysical data. In this study, we present results of the first broad-band magnetotelluric profile crossing the Mérida Andes and the Maracaibo and Barinas–Apure foreland basins on a length of 240 km. Geoelectrical strike and dimensionality analysis are consistent with 1-D or 2-D subsurface structures for the sedimentary basins but also indicate a strong 3-D setting for the Mérida Andes. Using a combination of 2-D and 3-D modelling we systematically examined the influence of 3-D structures on 2-D inversions. Synthetic data sets derived from 3-D modelling allow identification and quantification of spurious off-profile features as well as smoothing artefact due to limited areal station coverage of data collected along a profile. The 2-D inversion models show electrically conductive basins with depths of 2–5 km for the Barinas-Apure and 2–7 km for the Maracaibo basins. A number of resistive bodies within the Maracaibo basin could be related to active deformation causing juxtaposition of older geological formations and younger basin sediments. The most important fault systems of the area, the Boconó and Valera Faults, cross-cut the Mérida Andes in NE–SW direction along its strike on a length 400 km and N–S direction at its centre on a length 60 km, respectively. Both faults are associated with subvertical zones of high electrical conductivity and sensitivity tests suggest that they reach depths of up to 12 km. A sizeable conductor at 50 km depth, which appears consistently in the 2-D sections, could be identified as an inversion artefact caused by a conductor east of the profile. We speculate the high conductivity associated with the off-profile conductor may be related to the detachment of the Trujillo Block. Our results partially support the 'floating orogen hypothesis' developed to explain the geodynamic evolution of western Venezuela and they highlight the relevance of the Trujillo Block in this process.

Key words: South America; Magnetotellurics; Continental tectonics: strike-slip and transform.

1 INTRODUCTION

The Venezuelan Andes (Mérida Andes, MA) are part of a mountain chain extending from Ecuador, across Colombia and into western Venezuela. They started forming in the Early Miocene (Audemard & Audemard 2002) due to the interaction of three tectonic plates: Nazca to the west, Caribbean to the north and South American to the south (Fig. 1). The overall tectonic settings are complicated as the Caribbean Plate, being abnormally light, tends to override the South American Plate, thus not conforming with normal oceanic–continental collision (James *et al.* 2009).

As many aspects of the tectonic evolution and the deep lithospheric structures are still disputed, predominantly due to lack of deep geophysical data, the Integrated Geoscience of the Mérida

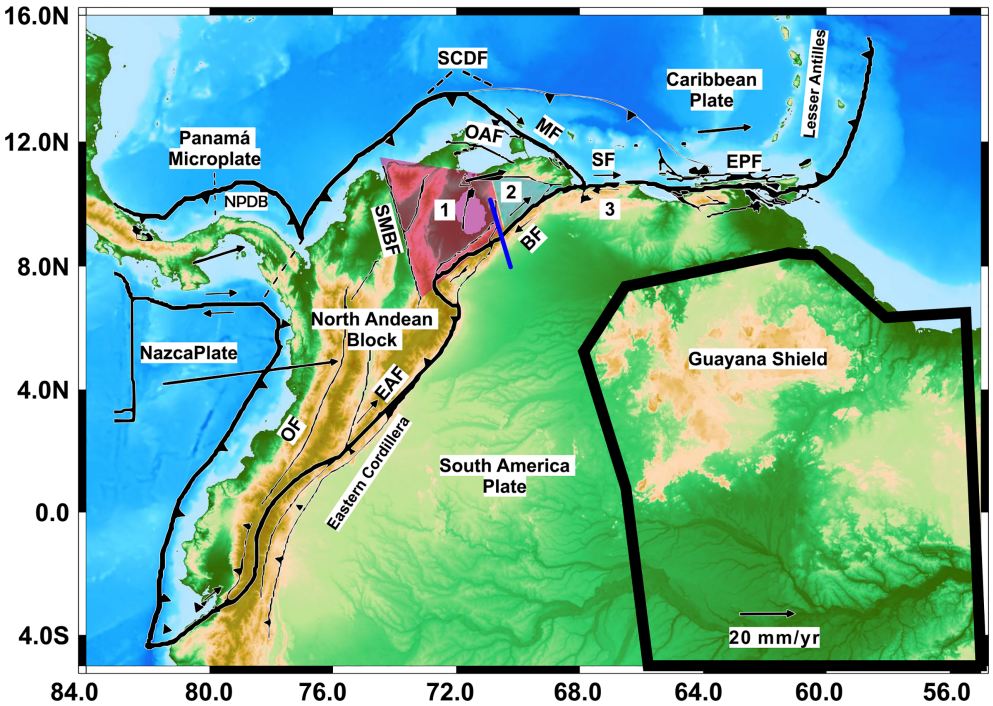

Figure 1. Schematic geodynamic setting of northwestern South America (modified from Pérez *et al.* 2018). The blue line indicates the position of the MT profile. Abbreviations: NPDB, Northern Panamá Deformation Belt; OF, Oriente Fault; EAF, East Andean Fault; SCDF, South Caribbean Deformed Belt; MF, Morrocoy Fault; OAF, Oca–Acón Fault; BF, Boconó fault; SMBF, Santa Marta–Bucaramanga Fault; SF, Sebastian Fault and EPF, El Pilar Fault. 1 – Maracaibo Triangular Block (MTB, limited by SMBF-BF-OAF), 2 – Trujillo Triangular Block (TTB) and 3 – Coastal Cordillera. Relative motion vectors compiled by (Pérez *et al.* 2018). Topography and bathymetry after G1.

Andes Project (the GIAME project, Spanish acronym) was initiated in 2013. The main objective of the project was to image the MA on a lithospheric scale and to develop a dynamic model of their evolution by integrating wide-angle seismic, magnetotelluric and potential field data.

In this paper, we report on the first regional magnetotelluric (MT) data set, acquired along a 240-km-long profile that crosses from south to north the Barinas–Apure basin (BAB), the central part of the MA, and the Maracaibo basin (MB). The MT method is used to derive the electrical conductivity structure within the Earth from depths of a few tens of metres to the upper mantle (Vozoff 1991).

The geodynamics of western Venezuela are dominated by the eastward movement of the Caribbean plate and the escape of the North Andean Block (e.g. González de Juana *et al.* 1980; Kellogg & Bonini 1982; Yrigoyen & Urien 1988; Audemard 2003; Duerto *et al.* 2006; Monod *et al.* 2010; Arnaiz-Rodríguez *et al.* 2011; Dhont *et al.* 2012; Pérez *et al.* 2018). As a part of the North Andean Block, the evolution of the MA is thought to be controlled by flat subduction of the shallow (∼40 km) Caribbean slab under northwestern Venezuela (Audemard & Audemard 2002; Monod *et al.* 2010; Mora *et al.* 2017). MT studies of orogens often revealed complex resistivity structures, typically associated with active deformation (see Unsworth 2009; Brasse 2011, and references therein). Particularly zones of high electrical conductivity are often associated with major fault zones or detachment zones in the mid- and lower-crust (e.g. Unsworth & Bedrosian 2004; Ritter *et al.* 2005; Becken *et al.* 2011; Meqbel *et al.* 2014). High conductivity in active tectonic regimes is often explained with fluids in fault systems and/or fluids derived from remineralization reactions of hydrous minerals (e.g. Jones 1993; Boerner *et al.* 1998; Jones *et al.* 2005; Ritter *et al.* 2005; Becken *et al.* 2011; Meqbel *et al.* 2016).

The results presented here show the first deep geoelectric images of western Venezuela. With the MT data, we can clearly distinguish between generally more conductive foreland basin structures and resistive domains associated with the MA. But we also find evidence for narrow, deep reaching zones of high electrical conductivity, which appear to be associated with major fault systems of the MA.

An in-depth examination of these zones of high conductivity, their spatial resolution and correlation with tectonic features is a major focus of this paper. Since data coverage is primarily along a single profile, we rely on the two-dimensional inversion of the data. The dimensionality and directionality analyses of our data suggest, however, that only the northern and southern parts of the data set are generally consistent with 1-D/2-D subsurface structures. They indicate strong 3-D effects, particularly for the MA section. It is therefore essential to investigate and quantify how 3-D effects affect the outcome of 2-D inversion.

2 GEODYNAMIC EVOLUTION AND GEOLOGICAL SETTINGS

The MA are the most prominent feature of Western Venezuela. They developed as a transpressional orogen due to E–W low-angle convergence between the Maracaibo triangular block and the Guyana Shield (Audemard & Audemard 2002). The MA also form the eastern boundary of the North Andean Block (Fig. 1) which moves towards the NNE by approximately 1.5 cm yr^{-1} with respect to South America (Pérez *et al.* 2018) since the Late Miocene (Audemard 2014).

The formation of the MA is related to the geological evolution of the northern part of the South American continent (La Marca 1997). According to Yrigoyen & Urien (1988), the geodynamic

settings that shaped western Venezuela began with the separation of the supercontinent Pangea. In the Precambrian to early Palaeozoic, the South American Plate was initially displaced to the west and then northwestward, thereby forming what came to be the central parts of the MA as well as the basement of western Venezuela. Based on the Pacific model for the formation of the Caribbean Plate (e.g. Pindell *et al.* 2005), the westward divergence of the South American Plate towards the Nazca Plate, formed the Caribbean Large Igneous Province off Colombia's Pacific coast at the end of the Jurassic period (Yrigoyen & Urien 1988). As the Caribbean Large Igneous Province was thicker and less dense, it overrode the surrounding oceanic plates. The divergence of North American and the South America plates provided a path for the Caribbean Large Igneous Province to progress northwards.

The migration of the Caribbean Large Igneous Province in the Cretaceous started the formation of the current Caribbean Plate (Hauff *et al.* 2000). Approximately 100 Ma, the northern part of the South American Plate formed the bottom of the Proto-Pacific Ocean, which facilitated the formation of the MB and BAB. From the Early Cretaceous to Mid-Eocene, sediments were deposited in a setting of an extensive passive continental margin. The Cretaceous formations, mostly marine sandstone, shale and limestone, are the main source rocks of the sedimentary basins (De Toni & Kellogg 1993).

The divergence between the North and South American plates, also created the space for the Caribbean Plate to move towards its current location. This diachronous oblique convergence between Caribbean arc terranes and the South American continental margin from Late Cretaceous to the present formed west to east younging patterns of thrusts, lateral ramp faults and foreland basins onshore (Escalona & Mann 2006b). A collision of the Panama Arc with the South American plate in the early Miocene caused uplift of the MA and formed other major mountain chains, including the Perijá range at the western boundary of the MB (Fig. 2). Since the Late Miocene, the deformation rate is partially controlled by the escape of the North Andean Block. The interaction between the Caribbean Plate and the North Andean Block favours the formation of a series of right-lateral strike-slip fault zones which reach its north-eastern boundary at the triple junction between the Boconó (BF), Morrocoy (MF) and San Sebastian (SF) fault systems (Pérez *et al.* 2018, Fig. 1).

Uplift of the MA accelerated during the Plio-Quaternary due to transpression related to oblique convergence between two independent blocks belonging to the South American plates: the Maracaibo triangular block to the west, and the Guyana shield to the east (Dhont *et al.* 2005). This process led to an inversion of a pre-existing Jurassic graben, exposing crystalline and metamorphic rocks of Precambrian to Palaeozoic age in the central part of the MA. Uplift of the MA separated the MB and BAB, and subsequent erosion filled them with Neogene to Quaternary sediments. The relative convergence between the Maracaibo triangular block and the Guyana shield, caused the Trujillo triangular block to start moving towards the NE (Dhont *et al.* 2005). This block is bounded laterally by both the BF and Valera fault (VF) systems.

The relative movement along the eastern flank of the Maracaibo triangular block resulted in the formation of several hills defining the eastern boundary of the MB. It also created deformation structures like synclines and anticlines and shale diapirism towards the edges of the basin (Escalona & Mann 2006b). Most of the regional and local deformation processes took place north of the MA. Consequently, the BAB presents less evidence of current deformation and is structurally simpler than the MB.

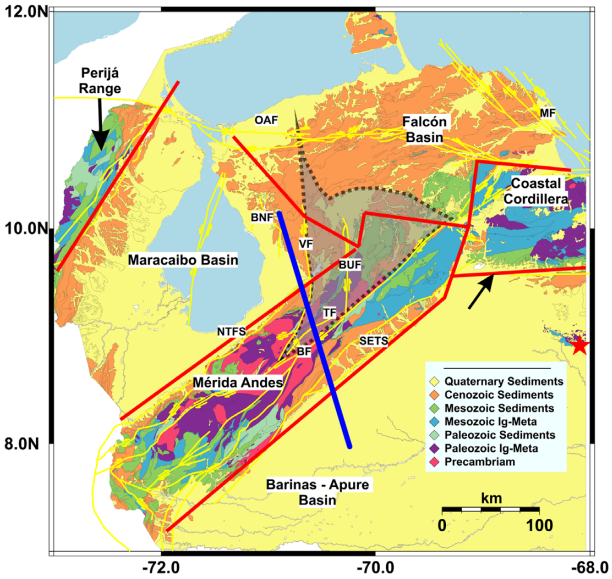

Figure 2. Major tectonic units of western Venezuela based on a simplified geology after Hackley *et al.* (2006). The red lines mark the limits of the major surface structures following the classification of Urbani (2017). A simplified distribution of the Quaternary fault system are marked in yellow lines (modified from Audemard *et al.* 2006). The blue line indicates the location of the MT profile. The translucent grey area marks the position of the Trujillo Block. The red star marks the location of the remote reference MT station. Abbreviations: OAF, Oca-Acón Fault System; MF, Morrocoy Fault; BNF, Burro Negro Fault; VF, Valera fault; TF, Tuñame Fault; BF, Boconó fault; BUF, Burbusay Fault; NWTS, Northwestern thrust system (also known as Las Virtudes thrust system) and SETS, Southeastern thrust system.

Fig. 2 gives an overview of the regional geology and the location of the MT profile in the study area. The MT profile crosses the central part of the BAB, the northern section of the MA and extends until the eastern boundary of the MB.

Two distinctive features of the BAB are the plains (or Llanos) and the foothills. The stratigraphic section of this sedimentary basin comprises as much as 5 km of Aptian through Pleistocene sediments (Callejón & von der Dick 2002). The Cretaceous section consists of sandstone, limestone and shale. A Tertiary section with a major oil-producing interval, characterized by the Andean uplift is represented by the molassic sequences of sandstone, shale and conglomerates. These sediments rest discomformably over a pre-Palaeozoic basement of igneous and metamorphic rocks, exposed by the uplift of the MA (Callejón & von der Dick 2002).

Across the MA, the southern foothills are defined by a NE–SW trending flexural scarp facing SE, known as the Southeastern thrust system which extends for over 200 km and reaches a maximum height of 300 m above the low topography of the Llanos plains (Audemard 1999). The thrust system displays active flat-ramp thrust faults, triangular zones and associated piggy-back basins filled with Late Miocene–Quaternary molassic deposits (Audemard & Audemard 2002). The northern foothills of the MA are defined by a major NW verging thrust sheet, the Las Virtudes overthrust (or NWTS in Fig. 2), which brings Precambrian and Palaeozoic metamorphic rocks in contact with Tertiary rocks at the mountain front.

The most prominent tectonic features of the MA are the Boconó and Valera fault systems. According to Dhont *et al.* (2005), the BF is a NE-trending 500-km-long fault which cross-cuts the belt longitudinally approximately along its axial part. Age estimates for this

structure vary among authors, including late Miocene (Audemard & Audemard 2002), Pliocene (Dewey 1972) and Pleistocene (Schubert & Vivas 1993). The ∼240-km-long left-lateral strike-slip VF (170 km in its four segments according to Audemard *et al.* (2000)) is another main fault cross-cutting the northern part of the MA. It has been described as a normal synsedimentary fault during the Mio-Pliocene (Kerher 1925; Garcia & Campos 1977), and it is reported to have been reactivated as a sinistral strike-slip fault in the Quaternary (Soulas *et al.* 1985).

The northern segment of the MT profile crosses the southern and eastern boundaries of the MB. The MB is reported to be an asymmetric trough that contains up to 12 km of carbonates and shale of late Cretaceous to Eocene age (De Toni & Kellogg 1993). However, as a result of the uplift of the MA and the Perijá Range, to the south and west, and the active faulting of the Burro Negro Fault (BNF) and the VF, to the east, the maximum depth of the basin lies between 2 and 5 km (Escalona & Mann 2003, 2006a). In the Palaeogene and late Neogene, regional shortening folded and thrust Palaeozoic basement rocks, Mesozoic-Cenozoic carbonates and clastic rocks were exposed by the uplift of the MA at the eastern boundary of the MB (Duerto *et al.* 2006).

3 MAGNETOTELLURIC DATA SET

3.1 Data acquisition and processing

For the MT method (Tikhonov 1950; Cagniard 1953), naturally occurring EM fields are used to investigate the electrical conductivity structure of the earth (Vozoff 1991). Electromagnetic current systems from worldwide thunderstorm activity and the interaction of solar activity with the ionosphere induce currents into the electrically conductive Earth. MT data are acquired by measuring temporal variations of the electric (E) and magnetic (B) field at the surface, using non-polarizing electrodes and induction coil magnetometers. At each site, two electric dipoles in N–S and E–W directions, and three magnetic field components oriented in N–S, E–W and vertical direction are measured. Time series of horizontal E and B fields are used to calculate the impedance tensor (Z), a complex tensor that is often presented as apparent resistivity (ρ_a) and phase (φ). The relationship between the recorded vertical magnetic field and the two horizontal magnetic fields yields the vertical magnetic transfer function (VTF), usually presented as induction vectors.

The MT data for this study were collected between March and April 2015. A total of 72 MT stations were deployed along a 240-km-long profile across the central part of the MA (Fig. 3). The profile follows an NNW–SSE direction. Initially planned to be almost perpendicular to the MA and its major fault systems, the profile's final position resulted from a combination of accessibility and the locations of profiles of other geophysical methods acquired in the framework of the GIAME project. Station spacing varied between 3 and 5 km. Site distances in the MA were smaller to account for topography and to achieve a better coverage of fault systems and active deformation structures. The site distances were larger at both profile ends, along the MB and BAB, respectively.

This data set was collected in a broadband configuration, that is in a period range of 10^{-5} s to over 1000 s. Magnetic fields were recorded with Metronix MFS06/07/10 induction coils magnetometers and the electric fields with non-polarizing silver–silver chloride (Ag/AgCl) electrodes, supplied by the Geophysical Instrument Pool Potsdam (GIPP). Short period (high frequency) data were recorded in intervals: once a day for 10 min with a sampling rate of 4×10^{-5} s

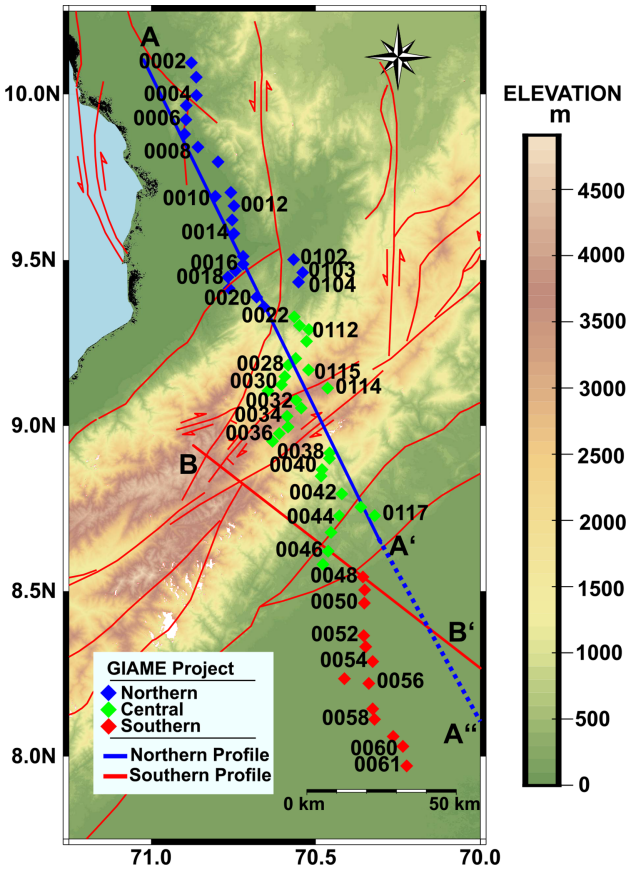

Figure 3. Elevation map with stations locations. Symbols next to the station labels are colour coded to differentiate northern (blue), central (green) and southern (red) subsets (see dimensionality and strike analysis). For clarity, most station labels with odd numbers were skipped. Blue and red lines indicate the virtual profiles (rotated perpendicular to geoelectric strike) used for subsequent 2-D inversions (see text). The dotted blue line is an extension of the northern profile considered in the 2-D inversion studies (see text). The red lines indicate Quaternary fault systems (from Audemard *et al.* 2006). Topography and bathymetry after G1.

(25 kHz), and for 10 min every 2 hr with a sampling rate of 8×10^{-4} s (1250 Hz). Long-period (low frequency) data were recorded continuously with a sampling rate of 0.02 s (50 Hz), and a minimum of 3 days recording per station. In addition, a station was installed about 300 km east of the profile (see Fig. 2) for remote reference processing (Gamble *et al.* 1979) and it was left recording for the entire acquisition period with the same sampling rates and recording intervals as the stations on the profile.

The MT transfer functions (Z and VTF) were estimated from the recorded time series using robust single site and remote reference processing routines of the EMERALD software package (Ritter *et al.* 1998; Weckmann *et al.* 2005; Krings 2007). It should be noted that the MT data were heavily affected by EM noise at different frequencies. The sources ranged from electric fences to the power grid, a hydropower plant and a number of small communities and small cities that could not be avoided. As security measures, stations were installed in between the limits of farms and in enclosed grasslands, which also influenced the data quality, despite collaboration with local landowners (e.g. switching off local power grids). To improve the signal to noise ratio we used notch filtering (based on Hanstein *et al.* 1986), successfully removing the 50 Hz peak and

its harmonics related to the power lines in Venezuela. Remote reference processing (*RR*, Gamble *et al.* 1979), where the measured horizontal magnetic field of a local and remote site are used simultaneously to eliminate uncorrelated noise, greatly improved the quality of the data between 10^{-1} and 10 s. Data quality could be further improved by using a frequency domain selection scheme (Weckmann *et al.* 2005) and a novel statistical approach for data pre-selection employing the concept of the Mahalanobis distance (MD) and the magnetic polarization direction to remove outliers and EM noise (Platz & Weckmann 2019).

Fig. 4 shows an example of the data quality and the improvement achieved by applying the processing steps described above. Apparent resistivity and phases are plotted together with the vertical magnetic transfer functions, presented as induction vectors. High quality data are expected to vary smoothly over period. Fig. 4(a) reveals that responses for Zxy and Zyx are scattered at mid and long periods (above 1 s) and show a deviation from the general trend. Distorted sections of the responses particularly for low periods ($<10^{-1}$ s) and between 1 and 100 s could be improved with the combination of time domain filtering and data pre-selection (Figs 4b and c). The novel processing approach based on the MD (Platz & Weckmann 2019) is very effective in removing noise. For the longer periods (>100 s) less data is available and therefore all statistical methods are less effective. Obvious outliers that were still present in the data after all processing steps were manually removed prior to inversions.

Due to the location of the study area near the Equator, we also examined the effect of the equatorial electrojet (EEJ, e.g. Reddy 1989). The EEJ is a non-uniform east west-flowing current system, which is active only during daytime. These current concentrations form in-homogeneous EM sources which violate the assumption that the primary EM field propagates downwards as a plane wave (Tikhonov 1950; Cagniard 1953), which is a prerequisite for the MT method. Using the same processing routines described above, we processed day-time and night-time data separately for three selected sites. Transfer function estimates of day-only and night-only processing differ by less than 5 per cent. Moreover, though being close to the equator, our study region is located at the northern edge of the region influenced by the EEJ (see Forbes 1981). Hence, we conclude that the effect of the EEJ can be neglected.

3.2 Dimensionality and strike analyses

To assess the inherent complexity of the MT data set, dimensionality and geoelectrical strike analyses were carried out. Dimensionality analysis describes the complexity of an area or its deviation from simple structures, such as a homogeneous or layered (1-D). The analysis of the impedance tensor makes it possible to differentiate between a subsurface dominated by a (regional 2-D) geoelectrical strike or by more complex (3-D) structures without a clear geoelectrical strike.

Phase tensor analysis (PT, Caldwell *et al.* 2004) was used to investigate the dimensionality of the study area. MT data is often affected by small scale conductive structures, that change direction and magnitude of the *E* field (Bahr 1988). These distortions are caused by charges accumulating at the boundaries of the small-scale structures, distorting the pattern of regional current flow in a localized area encompassing the structure (Caldwell *et al.* 2004). These frequency-independent distortions are known as galvanic distortions and can be represented as real matrices. Since PT are the ratio between the real and imaginary parts of the impedance tensor, the PT remain unaffected by distortion (Caldwell *et al.* 2004).

Phase tensors are second rank 2-D tensors that can be characterized by their coordinate invariants and represented graphically by an ellipse (e.g. Bibby 1986). The maximum and minimum PT values are used to construct the major and minor axes of the ellipses, respectively, and the tensor skew angle (β) serves as a measure of the tensor asymmetry (see Caldwell *et al.* 2004; Booker 2013). In practice, the skew angle (β) is used as an indicator for the complexity of the underlying geological structures, with values above $\pm 3^\circ$ generally considered to be incompatible with 1-D/2-D assumptions (Caldwell *et al.* 2004; Booker 2013). For the 1-D case, the ellipses assume a circular shape with β values between $\pm 3^\circ$. In the 2-D case, β values stay between $\pm 3^\circ$, but the PT form ellipses with their major or minor axis aligned with the preferred electric current direction, the geoelectrical strike.

The induction vectors (IV), which are calculated from the vertical magnetic field through the VTF, indicate the presence or absence of lateral variations of the conductivity structure (Weaver 1994). For the ideal 2-D case, the real and imaginary parts are collinear and perpendicular to strike direction. In the Wiese convention (Wiese 1962), IV point away from conductive structures, thereby indicating their geoelectric strike directions. PTs are therefore used in combination with IV to decipher the structural complexity of the subsurface.

A regional geoelectrical strike is present in the data when the horizontal dimensions of a conductivity anomaly are comparable with the depth of penetration (Bahr 1988). To calculate a geoelectrical strike direction we also used the tensor decomposition method of Becken & Burkhardt (2004). This method estimates the geoelectrical strike based on an ellipse parametrization of the columns of Z or telluric vectors (Bahr 1988). The ellipticity of the telluric vectors are rotationally variant and vanish for 2-D conditions if data are rotated to the regional strike direction. Therefore, the regional strike direction can be determined by minimizing the sum of squared ellipticities weighted with their variances by rotating the coordinate system (Becken & Burkhardt 2004). This procedure can be carried out in single and multisite modes. In single-site mode, each station is analysed individually for a given period range and a regional strike angle is found per site. In the multisite mode, a strike angle is sought that best fits all selected stations in the given period range. The regional geoelectrical strike direction derived by tensor decomposition methods has an inherent 90° ambiguity, which can be solved by considering the IV.

Fig. 5 shows maps of the PTs and IV for a range of periods, the depth of investigation generally increases with increasing period. Colour scale of the PTs allows identification of 1-D/2-D and 3-D structures in the subsurface. The results of this dimensionality and directionality analysis suggests a grouping of the stations into northern, central and southern sections (see Fig. 3). The sections roughly coincide with the MB, MA and foothills, and the BAB.

The central section in Fig. 5(a) shows β values exceeding the 1-D/2-D limits ($\pm 3^\circ$) and IV with strongly variable directions and significant magnitudes. Such variations are expected in the vicinity of a strong conductivity contrast in the subsurface. Comparison with the Quaternary fault systems (red lines in Fig. 5 after Audemard *et al.* 2006) of this area hints at the BF system, with its many actively deforming fault strands, as a possible source for such a conductivity contrast. The IV in Figs 5(a) and (b), however, point clearly to the W and SW, parallel to the BF, reacting to the presence of a good conductor east of the profile, which bears a bigger influence on the IV than the fault systems.

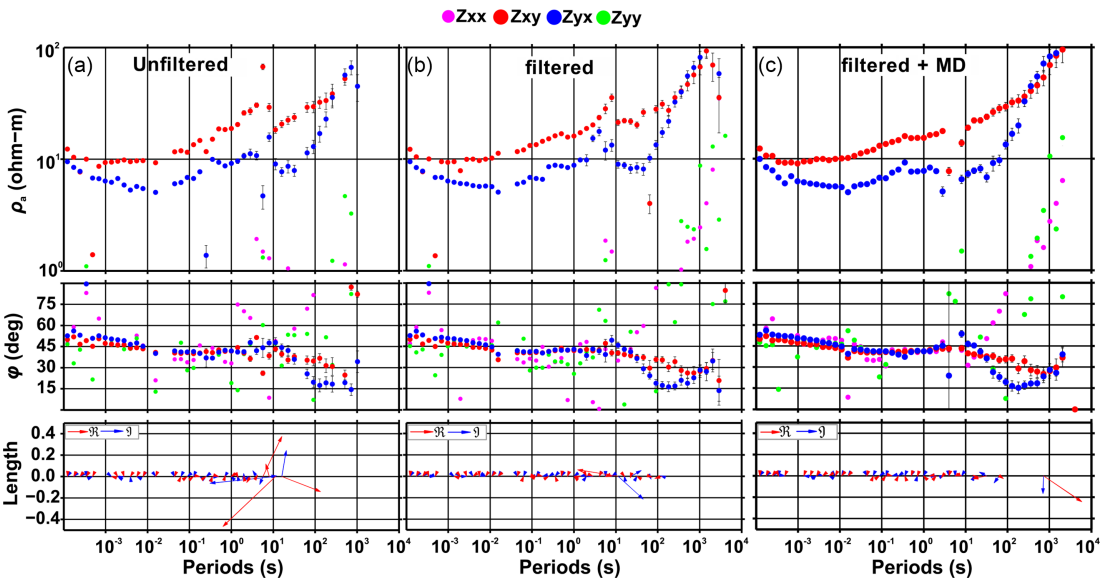

Figure 4. Comparison between robust processing of (a) unfiltered data, (b) time domain filtered data with remote reference processing applied and (c) in addition using the MD processing and magnetic polarization criteria (Platz & Weckmann 2019) for all four elements of the impedance tensor Z. The top row shows apparent resistivity, the middle row phases and the bottom row real (red) and imaginary (blue) parts of the induction vectors in the Wiese convention (Wiese 1962) of station 0002.

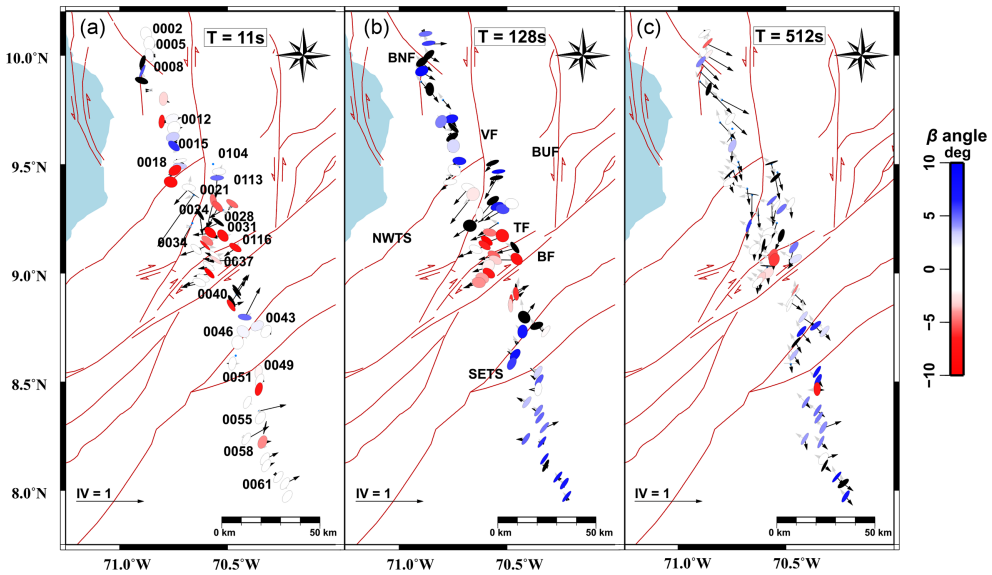

Figure 5. Phase tensors (coloured ellipses) and induction vectors (black arrows; real part) along the profile for periods of (a) 11 s, (b) 128 s and (c) 512 s. The red lines indicate Quaternary fault system [from Audemard *et al.* (2006), see Fig. 2 for abbreviations]. The filling colours of the ellipses represent the skew angle (β). Values over $\pm 10^\circ$ are depicted in black, white ellipses indicate values between $\pm 3^\circ$. Ellipses are normalized by their major axes.

As stated above, the northern and southern sections (MB and BAB) are generally associated with lower β values and small IV, however, PT shapes are hardly circular. The low β values are consistent with 1-D sedimentary structures and layering of stronger or weaker consolidated sedimentary material. Depending on the porosity and the abundance of (saline) fluids, sedimentary sequences can be expected to be conductive, typically in the range 1–100 Ωm; while the underlying crystalline basement can be expected to be resistive, typically exceeding 1000 Ωm (e.g. Telford *et al.* 1977). The pronounced elliptical shape in combination with the colouring of the PTs at periods longer than 100 s (Fig. 5b) can be related to deformation. Most of the deformation is observed on the northern flank of the MA, which coincides with changes in orientation of the PTs over the MB, rotating from an N–S to E–W direction of the major axis of the ellipses. Their orientation may be related to the proximity to the traces of the major fault systems such as VF, Las Virtudes thrust system and the Burro Negro Fault (see Figs 2 and 5a). Over the BAB (Figs 5a–c), PTs directions are subparallel to the fault systems (SETS and BF).

At longer periods (>100 s, Fig. 5c), most IVs point away from the highly conductive water of the Caribbean sea (roughly 100 km north of station 0002), also described as the coast effect (e.g. Parkinson 1959). Overall PT and IV show a growing structural complexity with period.

The results of the tensor decomposition analysis of impedances after Becken & Burkhardt (2004) are presented as rose diagrams in

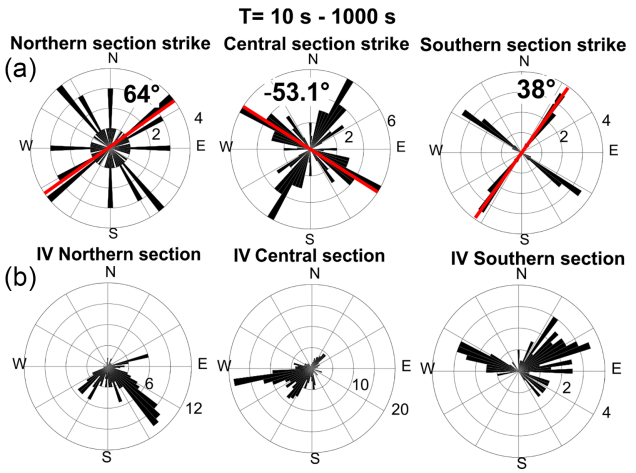

Figure 6. Rose diagrams of (a) single site multifrequency geoelectrical strike estimates (calculated after Becken & Burkhardt 2004) and (b) induction vectors (in Wiese convention) for the northern (left-hand panel), central (middle panel) and southern (right-hand panel) sections for periods between 10 and 1000 s. Clear tendencies for a regional strike can be seen in all three subsections. The strike values per section based on the multisite analysis are marked by red lines. The IV were used to solve the 90° ambiguity of the geoelectrical strike.

Fig. 6. Fig. 6(a) shows the distribution of derived strike angles for each section, for periods between 10 and 1000 s. For comparison, Fig. 6(b) shows rose diagrams of the IV in the same period range. Generally, the tensor decomposition analysis of the southern and northern sections indicates subsurface structures consistent with 2-D conditions. The central section appears to be more 3-D and without clear regional strike directions.

For the northern section, the strike analysis reveals two preferred directions NW–SE and its perpendicular NE–SW (Fig. 6a). As the IVs are SE oriented (Fig. 6b), the preferential strike direction for this section is ∼68° (red line in Fig. 6a). For the southern section, the IV are generally small and scattered (Fig. 6b), thus they could not be used to solve the 90° ambiguity of the strike analysis. However, in a 2-D case, the direction of the major axis of the PT is aligned parallel or perpendicular to the strike of the (regional) conductivity distribution (Caldwell *et al.* 2004). In Figs 5(a)–(c) the major axes of the PT show a NE–SW direction, subparallel to the fault systems in the area, hence we determine ∼38° as the geoelectrical strike (Fig. 6a). In both cases, the ellipticity values were consistently below 0.1.

In a 3-D environment, there is generally no regional geoelectrical strike, but for the MA a dominant strike direction can be identified which is useful for comparison with the regional geology. For the central section, a strike of –53.1° was found, almost perpendicular to the BF with ellipticity values reaching 0.5. The IV of the central section consistently point to the west (Fig. 6b). These observations together with the results of the PT (Fig. 5) support the 3-D character of this section and suggest a conductive structure east of the profile.

In summary, 2-D inversion may be useful to partly explain the most prominent features of this data set, particularly those located under the southern and northern sections. However, more complicated (i.e. 3-D) conductivity structures may be missed or might appear as artefacts in the 2-D inversion images. To explain the differences in the data set we grouped the stations in northern and southern profiles, both profiles include the stations of the central section. The blue AA' and the red BB' lines show the extension of the profiles in Fig. 3. Many examples exist in the literature which demonstrate that 2-D inversion of data sets with 3-D influences can still be useful (e.g. Ledo 2005; Becken *et al.* 2008; Becken & Ritter 2011; García Juanatey *et al.* 2012; Tietze & Ritter 2013). However, a deeper understanding of the influence of the observed off-profile features in the 2-D models is required.

4 INFLUENCE OF OFF-PROFILE FEATURES ON 2-D INVERSION

To study which structures can be robustly recovered as well as to estimate the influence of off-profile features, we decided to compare inversions of synthetic data derived from 3-D forward modelling and results obtained from 2-D inversions of these synthetic data.

4.1 3-D model and synthetic data set

A synthetic data set was generated using ModEM (Meqbel 2009; Egbert & Kelbert 2012), which is based on a discrete formulation of Maxwell's equations employing a finite differences approach. The 3-D models contain simplified regional geological and tectonic structures, as shown in Figs 1 and 2, including major regional sedimentary basins from western Venezuela, northern Colombia, and the Guyana shield (Fig. 7a). Approximate resistivity values, lateral and vertical extensions, as presented in Table 1, were taken from literature and regional studies (Telford *et al.* 1977; La Marca 1997; Escalona & Mann 2003; Chacín *et al.* 2005; Duerto *et al.* 2006; Urbani 2017).

The 3-D modelling grid consists of 152×92×132 cells in *x*-, *y*- and vertical directions (1789×1633×885 km^3). In the innermost part of the grid, horizontal cell sizes are 2.6 x 2.6 km^2 while cell sizes increase gradually to 225 km in the outer parts of the grid. For the top 5000 m, vertical cells have fixed values between 25 and 100 m. At 5000 m depth (below the sea level), the vertical dimensions of the cells increase gradually by a factor of 1.2. Topographic and bathymetric data are taken from the NOAA open database (Amante & Eakins 2009). The background resistivity is 500 Ωm. The Caribbean Sea is included with a resistivity of 0.3 Ωm and 5 km of sea sediments, with gradually increasing resistivity, were also considered.

Several model variations with different levels of complexity were tested, such as the inclusion of different fault systems and variations of bulk resistivity for the basins. Ultimately, only the major fault systems were considered for the inversion study, namely the BNF,VF, BUF and BF. Their resistivities were set to be at least 2 orders of magnitude lower than the background resistivity. This resistivity contrast allowed us to partially reproduce the IV and PT as observed in the measured data. An off-profile conductor was added to the east of the profile following the analysis of the IVs (see Figs 7a and c). The lateral and vertical extensions, as well as the resistivity of this conductor, were defined by testing different values. Its location was ultimately determined to simulate the observed dimensionality and directionality of the measured data (Figs 5 and 6) and using known tectonic features as boundaries (the BF, BUF and VF).

The synthetic data generated from the 3-D model in Fig. 7 has the same station distribution as the real data (see Fig. 3). The site locations, however, are slightly shifted to coincide with the centre of the horizontal cells of the 3-D model. The data set was obtained for a period range of 10^{-3} s to 1000 s, and 5 per cent of random Gaussian noise was added prior to 2-D inversion. Directionality analysis of the synthetic data set showed similar results to the measured data. Considering that it is a simplified model, the PTs β

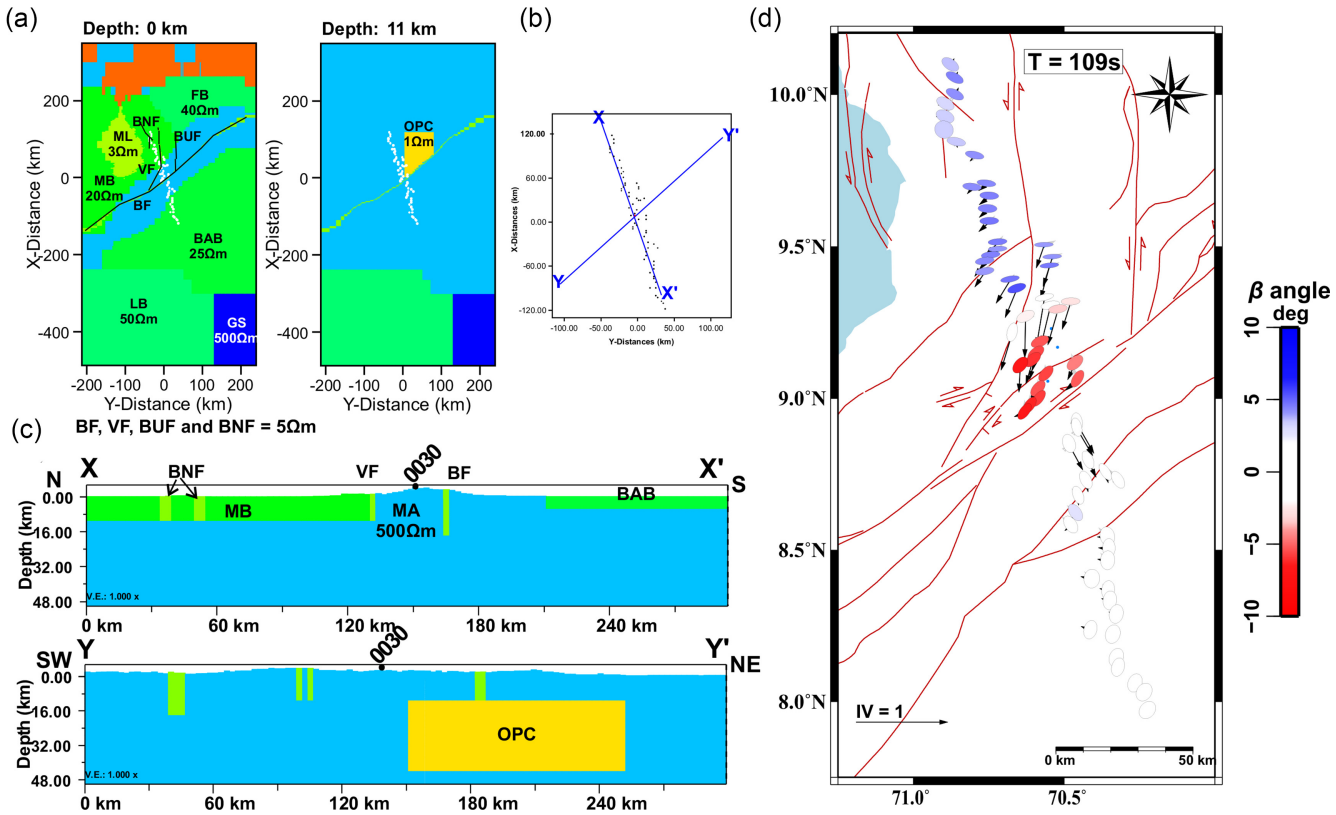

Figure 7. 3-D model presented in form of (a) two depth slices at 0 km and at 11 km depth. The surface slice also shows major fault systems in black. (b) Overview map showing the locations of both sections presented in (c) XX' and YY' are sections of the 3-D model with a maximum depth of 50 km depicting the locations and extensions of structures close to the profiles and the off-profile conductor, respectively. (d) Phase tensors (coloured ellipses) and induction vectors (black arrows; real part) along the main profile for the synthetic responses for a period of 109 s. Abbreviations: MB, Maracaibo Basin; ML, Maracaibo Lake; FB, Falcón Basin; BAB, Barinas-Apure Basin; LB, Llanos Basin; GS, Guyana Shield; OPC, Off-profile conductor; BNF, Burro Negro Fault; VF, Valera Fault; BUF, Burbusay Fault and BF; Boconó Fault.

Table 1. Estimated resistivity values and depths of major geological and tectonic structures used in the 3-D model in Fig. 7.

Geological feature	Resistivity (Ωm)	Maximum depth (km)
Maracaibo Basin (MB)	20	10
Falcón basin (FB)	40	3.5
Maracaibo Lake (ML)	3	0.04
Barinas - Apure Basin (BAB)	25	5
Llanos basin (LM)	50	15
Guyana Shield (GS)	5000	60
Fault systems (BF, BUF, BNF and VF)	5	10–15
Mérida Andes (MA)	500	–
Off-Profile Conductor (OPC)	1	11–41

values showed 2-D dimensionality for most of the data, while the IV (particularly in the central section) were pointing away from the OPC (see Fig. 7d). In general, PTs and IV showed their highest variations in magnitude and direction for stations in the vicinity of the fault systems. A regional geoelectrical strike of 36.9° (roughly the same direction as the BF) was found in the multisite analysis (Becken & Burkhardt 2004) for a period range of 10–1000 s. This indicated a stronger influence of the modelled BF in the synthetic data than in the observed data, where the geoelectrical strike was almost perpendicular to the BF.

4.2 2-D inversion set up

To solve the 2-D inverse problem, we used the finite elements (FE) code MARE2DEM (Key & Ovall 2011; Key 2016). MARE2DEM uses the fast Occam approach (a modification from Constable *et al.* 1987) to minimize the objective function and an automated adaptive mesh refinement based on a goal-oriented error estimator on unstructured triangular grids (Key & Ovall 2011). The input data are the rotated apparent resistivity (ρ_a) and phase (φ) curves, decoupled into transverse electric (TE) and transverse magnetic (TM) modes. In an ideal 2-D case, and if the coordinate system is aligned with

the strike direction, MT impedance responses can be decoupled into these two modes.

The synthetic stations were projected onto the northern and southern sections of the profile (see blue AA' and red BB' in Fig. 3) and rotated to the strike of the field data of each section (∼64° for the northern and 38° for the southern section, see Fig. 6a). Thereby we can also compare the synthetic data inversions with the 2-D inversion model of the measured data. The error settings for the 2-D inversions of synthetic data were 10–000 per cent for the apparent resistivities of TE, 10 per cent for those of TM and 1° for the phases of both modes, giving higher weight to phases than to apparent resistivities in inversion. Downweighting of apparent resistivities, in particular of the TE mode, is used in 2-D inversion to reduce the influence of static shift on the inverted resistivity structure. While the static shift of TM can be reproduced by small scale inhomogeneities just beneath or next to a station, 2-D models cannot replicate static shift for TE mode data (e.g. Jiracek 1990; Wannamaker *et al.* 1984, 1986). The rationale behind the choice of error floors, data rotation and projection is to use the same settings as applied to field data (see next section).

The starting models for the 2-D inversions presented in this section were also the same used for the field data, which are explained in detail in the next section. In general terms, they consisted of a 100 Ωm half-space with about 55 000 free elements, including topography and bathymetry and minimum edge lengths of 50 m growing with depth.

4.3 2-D inversion models

The resulting 2-D inversion models for the synthetic data set are shown together with the surface expression of structures from the original 3-D model in Fig. 8. Obtained conductivity anomalies are marked with C for conductors and R for resistors and the numbering is made to coincide with the 2-D inversions of measured data that are shown in the next section.

The 2-D inversions RMS for the northern and southern sections are 1.01 and 1.09, after 18 and 13 iterations (with an initial RMS of 18.4 and 21.6, respectively). For inverse problems where the data errors are accurately known and statistically well behaved (Gaussian distribution), an optimal misfit is an RMS of 1.05.

Comparison of the 2-D synthetic data inversion result of the northern section with a 2-D section of the true 3-D model shows similarities but also marked differences (Fig. 8a). Conductors labelled C1–C3 seem to represent the MB in our 2-D model, however, the recovery is not in the form of a homogeneous feature. Instead, the MB appears as a disrupted sequence of anomalies possibly caused by the uneven station distribution. The resistor R2 could represent the transition from a conductive basin to the west and a vertical conductor imaging a fault (in green colours) to the more resistive MA. Conductor C4 correlates with the VF as C5 does with the BF. In the true model, these structures have vertical dimensions of 10 and 15 km, respectively, whereas the inversion model shows a shallower concentration of higher conductivities in the upper 5 km. The BF is represented as a vertical structure, however, at approximately 8 km depth it seems to have produced a conductive horizontal structure extending towards the north. Below 10 km depth, the resistivities increase for the entire profile possibly related to the recovery of the background resistivity. This correlation is assumed given that there are no other structures present in the original model and the resistivity increment is recovered in an area with high model sensitivities.

The 2-D inversion of the southern section reveals more complex structures in the region of the MA than the corresponding section of the 3-D model comprises (Fig. 8b). Conductor C6 appears at the position of the BF, however, in the 2-D inversion the structure is bent and less deep reaching. In contrast, to the inversion result of the northern profile, which has a different orientation and, thus, a different cutting angle with the fault, the anomaly is now smeared out towards the south at its basis. The Conductor C9 coincides with the location of the BAB; as observed in profile (A) (Fig. 8a), resistivity values are lower than in the true model and the basin is not recovered as a contiguous layer due to the irregular site coverage. Along large parts of the profile, SE of the MA, the increase of resistivities at depth (>10 km) is recovered.

4.4 Influence of off-profile structures and profile orientation

Inversion models of both profiles contain structures which do not have an obvious correlation with structural features on the profile section of the true model (C8 and black circle in Figs 8a and b). These structures are artefacts caused by the 3-D nature of our synthetic data.

When attempting to interpret 3-D structures in 2-D inversions, the distance of the anomalous structures from the profile must be considered. Fig. 9 shows horizontal slices of the 3-D model illustrating the lateral geometries of the fault systems and the OPC together with the location of the profiles (Fig. 9b). The arrow heads indicate the position of observed resistivity anomalies in the 2-D models that do not directly correlate with on-profile features (*cf.* black circles and C8 in Figs 8). The arrows are approximately 10–15-km-long and perpendicular to the profiles; the length of the arrows is equivalent to the skin depth at periods of ∼10 s. Their main purpose is to illustrate the sensitivity radius around these anomalies and to identify potential 3-D off-profile structures which have been mapped into the 2-D inversion model.

A major 3-D feature and off-profile structure of the conceptual 3-D model is the OPC. Comparison of the inverted northern section with the true model suggests that the off-profile structure (OPC) to the east, appears as a conductive body underneath the MA (marked with a black line in Fig. 8a). To better understand the projection of the off-profile structure, we extracted the OPC from the 3-D model and created a new synthetic data set. This synthetic data set was subjected to 2-D inversion in the same way as for the original data set. These inversion models (not shown here) reproduced structures for the top 10 km of the models as seen in the original data models. In contrast, the deep anomaly > 30 km (marked with a black line in Fig. 8a) was not present in these 2-D inversions and, thus, can be clearly attributed to the OPC. Accordingly, blue arrows in Fig. 9(b) show that most stations along this profile are within 10–15 km of the OPC and affected by this structure. Structures highlighted with black circles in Figs 8a and b) were less conductive and closer to the surface. These anomalies appear to be a combination of the effect of the OPC and lateral resistivity variations between the resistive MA and the obliquely running MB and BAB. For the southern profile the red arrow in Fig. 9(b) suggests that the OPC might be too far away to have a considerable effect on the stations.

More local structures have also shown to contribute to the 3-D nature of the data. The Quaternary fault systems (black lines in Fig. 9a) cross the profiles at various angles, fault strands change directions and also cross each other at several (off-profile) locations. Conductor C1 in the northern profile correlates almost perfectly with the surface location of the BNF; notably, the BNF is the only structure which is crossed by the profile at an almost perpendicular angle. In contrast, the VF changes its direction from N35 °E to

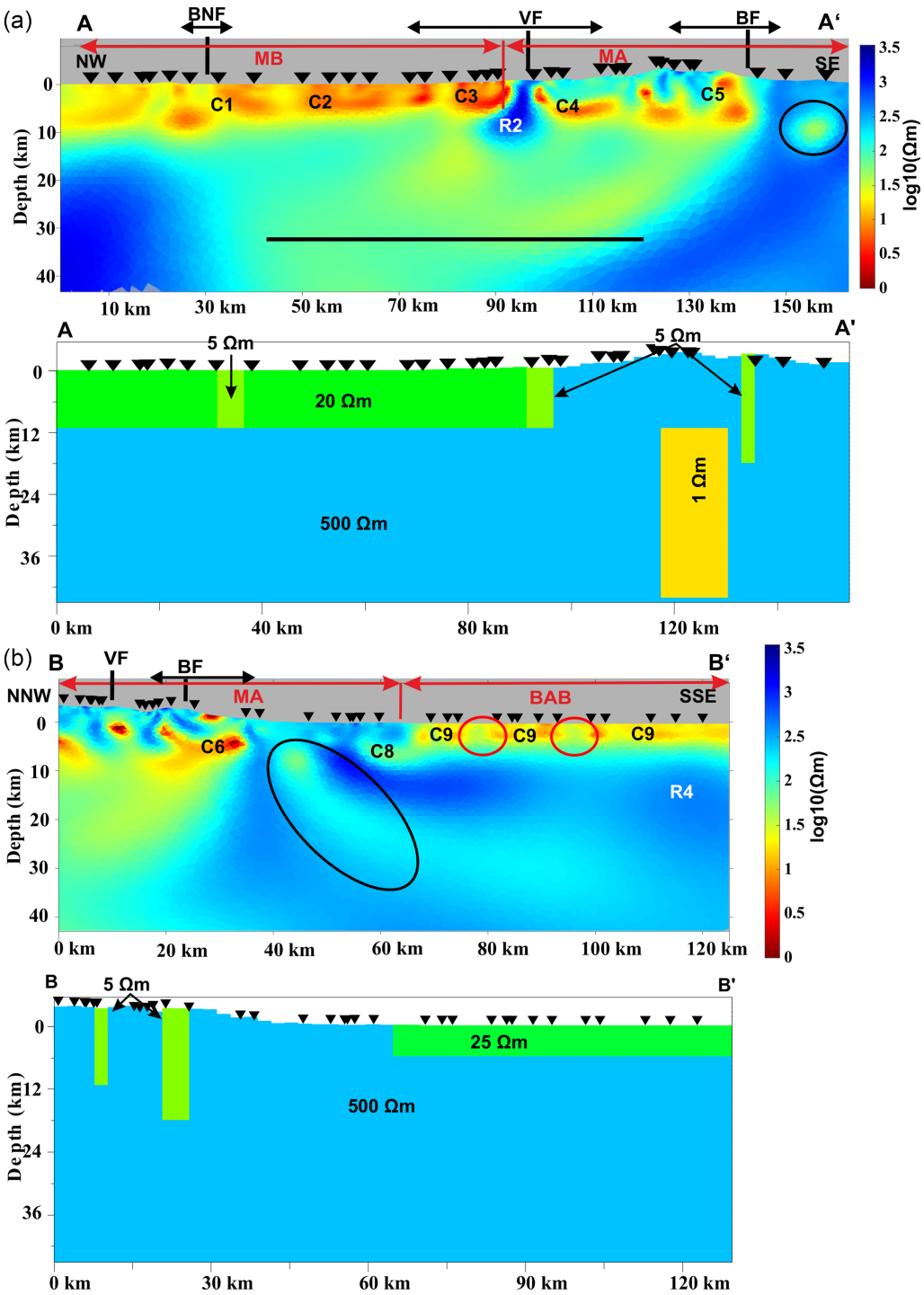

Figure 8. 2-D inversion results of synthetic MT data generated with 3-D forward modelling in comparison with corresponding sections of the 3-D model. (a) Northern and (b) southern profiles. The black triangles represent projected sites onto the profiles AA' and BB' (see Fig. 3). Surface expressions of the faults included in the 3-D model are marked with black bars and double headed arrows for their areas of influence (see Fig. 9). The approximate extensions of the sedimentary basins and the MA are indicated by red arrows (see also Fig. 7). The black line in A marks the top of the anomaly related to the off-profile conductor. The black circles mark spurious conductors caused by off-profile features and the red circles artefacts resulting from uneven station coverage (see text).

almost N when crossing the profile (yellow circle in Fig. 9a). Three stations east of the fault (102, 103 and 104) seem to be sensitive to the fault running almost parallel to the profile. This apparent mismatch of fault and 2-D model orientation likely explains the appearance of R2, C3 and C4 in the inversion model of Fig. 8(a). In the overlapping part of the southern section (Fig. 8b), which cuts the fault at a more perpendicular angle, significantly less artefacts occur around the VF.

It is worth nothing that the projection of the stations onto the profiles seems to have an influence on the shape and inclination of

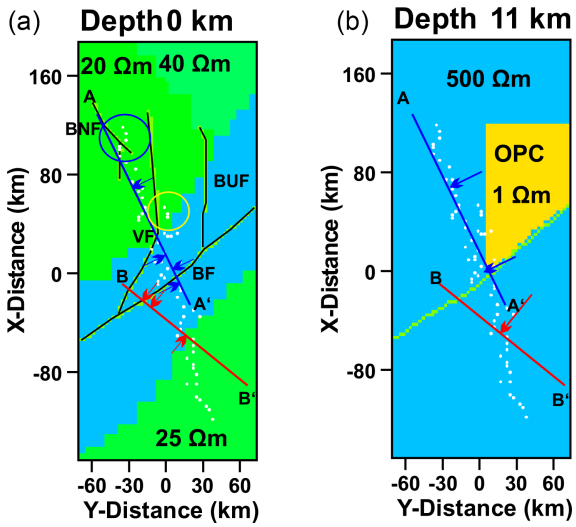

Figure 9. Zoomed view of the synthetic 3-D model highlighting the influence of off-profile structures presented in map view (a) at 0 km and (b) at 11 km depth. The blue and red arrows mark the lateral influence of the fault systems and the OPC in the northern (blue) and southern (red) profiles.The yellow circle marks stations affected by local 3-D effects (conductor C3, see text). The blue circle marks stations located above the BNF (see text).

the fault images. For example, stations north of the BF when projected onto the northern section stay north of the surface expression of the fault (Fig. 9a), explaining the northwards extension of the BF (Fig. 8a). Whereas, when the same stations are projected to the southern section, they are relocated south of the surface expression of the fault. Hence in the corresponding inversion model the BF appears smeared out southwards (Fig. 8b).

Overall, 2-D inversion images both lateral and vertical extent of the sedimentary basins reliably. The resistivity increase between stations in these regions indicates that the uneven station coverage and the regularization (smoothing) used foster the inclusion of separate bodies within the originally contiguous layers (C1-3 and C9). Conductive fault strands have been identified for both profile orientations. Where faults are crossed at an almost perpendicular angle by the profile, location and shape agree well with the true model. In contrast, images of faults running obliquely to the profile lines (VF/C4 and BF/C5 in profile A, BF/C6 in profile B, Fig. 8) resulted in more complexly shaped and offset structures in the 2-D inversion models. Therefore, the geometries of resistivity anomalies in the latter case have to be interpreted with caution.

5 2-D INVERSIONS OF THE MEASURED DATA

To interpret the northern and southern sections of our profile, all the stations of the profile were rotated to 64° and 38° (with the *y*-axis perpendicular to strike). This rotation effectively assigns the *yx*-component of impedance tensor to the TM mode and the *xy*-component to the TE mode.

The rotated sites were projected onto two profiles (blue and red lines in Fig. 3). Each profile includes the stations pertaining to its section and the sites from the central section for overlap. The profiles were centred on stations 0020 and 0048, respectively. The station distribution and profile location aim is to reduce the effect of station projections and large differences in topography.

5.1 2-D inversion setup

Input data for 2-D inversion are the rotated apparent resistivity (ρ_a) and phase (φ) curves recorded in the period range from 0.001 to 1000 s with 7 periods per decade, and the data were interpolated to account for masked responses. Since small scale near-surface heterogeneities can cause distortion and static shift, which affects the apparent resistivity curves but not the phases (e.g. Jiracek 1990), they have to be addressed in the inversion. For the TM mode, the inversion will normally handle static shift by inserting small conductivity anomalies directly beneath the affected stations. To accommodate static shift in the TE mode, a high error floor is normally set to the respective apparent resistivities. We tested a broad range of error floors for TM and TE mode resistivities and finally chose values of 20 and 10 000 per cent, respectively; phases are free of static shift and errors were set to 1.5° for both modes. Error floors < 20 per cent for TM resistivities massively increased spurious artefacts in the near-surface to accommodate for static shift. With an error of 10 000 per cent, TE resistivities are basically excluded from the inversion, similar results have been reported in other studies (e.g. Sass *et al.* 2014; Kütter *et al.* 2016; Muñoz *et al.* 2018). Consideration of TE apparent resistivities in the inversion with smaller errors, however, resulted in laterally smeared structures where major units, and in particular faults, are crossed obliquely by the profiles. TE apparent resistivities could have been omitted completely but were kept with high errors for convenience. Inversion tests using only phases and TM resistivities effectively gave the same results. For the inversion of conceptual data, we were able to use smaller errors. Yet, the synthetic data contain only 5 per cent noise, are free of galvanic distortion and are overall less affected by 3-D structures (particularly at short periods).

As mentioned before, the VTF over the BAB and MB were generally small and poorly resolved for short periods. Whereas over the MA, they show better quality but seemed to be more sensitive to off profile structures. Particularly, at longer periods, induction vectors generally became larger but were also influenced by off-profile features. All attempts to include them in the inversion seemed to add spurious surface conductors. Therefore, we did not include the induction vectors in the 2-D inversions.

Inversion parameters were tested by experimenting with a range of values for background resistivity, grid sizes, detail of topography, the inclusion of the Caribbean Sea to account for the coast effect, regularization and the trade-off parameter that weights regularization against data fit. The starting model was a 100 Ωm half-space, which included a simplified topography and bathymetry from the NOAA database (Amante & Eakins 2009); the sea water resistivity was set to 0.3 Ωm. The subsurface was discretized with 55 000 cells. To force cell sizes of the finite element grid to mainly grow with depth, we defined seven horizontal planes between 100 m and 120 km below the surface between each of which cell sizes were kept constant. Edge lengths varied from 50 m for the top layer to 5 km in the deeper regions. The trade-off parameter was set to 5 and the weight between horizontal and vertical smoothness to 3.

5.2 2-D resistivity models and data fit

The 2-D inversion models from the northern and southern sections are presented in Fig. 10. The superficial extent of the basins, the MA and the fault systems at the surface with respect to the projected section are marked on top of the models. In both profiles, the sedimentary basins are imaged as (series of) conductive (< 3 Ωm) bodies. Models suggest a depth of 5 km for the BAB and 5 –7 km

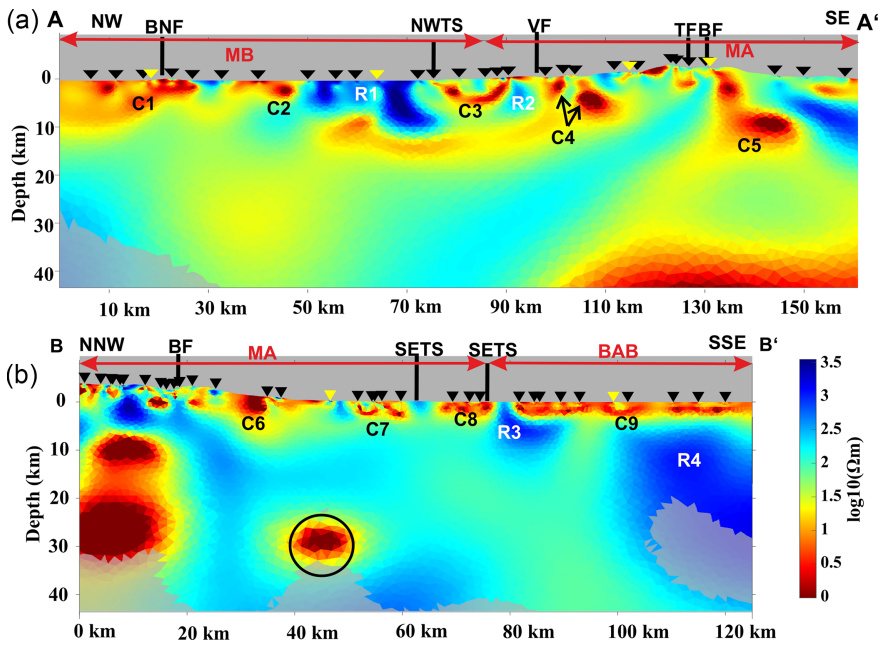

Figure 10. 2-D inversion results for (a) the northern (rotated by –116°) and (b) the southern section (rotated by –142°). The location of the sections is shown in Fig. 3 (blue AA' and red BB' lines). Surface expressions of fault systems are highlighted with black lines, while the surface extensions of the MB, MA and BAB are depicted as red arrows. The grey shaded area represent sections of the model with sensitivities lower than $10^{-6.5}$ and 10^{-6} (see Fig. 13). Yellow triangles mark the position of the stations shown in Fig. 12 (with 0005 as the northernmost and 0057 as the southernmost stations).

Table 2. RMS of the 2-D inversions of field data for the northern and southern section, for the TE and TM mode apparent resistivities (ρ_a) and phases (φ).

	Northern	Southern
TEφ	2.02	2.28
TMρ_a	0.79	1.40
TMφ	1.22	1.38

for the MB. The subsurface of the MA appears mainly as resistive intersected by various good conductors. The latter seem to be spatially related to the Boconó fault system. Due to the strong 3-D effects observed on the stations located at the MA (see Fig. 5) and the different strikes of each 2-D section, we observed considerable differences on the anomalies recovered in this area. As discussed in the previous section, the position and shape of the conductivity anomalies associated with the fault systems and the OPC, are influenced the projection of the stations onto the profile and the data rotation. The resistivity features and their geological implications will be discussed in detail in Section 5.4.

Inversion of the northern and southern sections converged to RMS values of 1.25 (initial 22.98) and 1.67 (initial 41.53) within 32 and 29 iterations, respectively. After reaching their minimum RMS inversion were allowed to 4 and 8, smoothing iterations in phase 2 of the fast Occam algorithm. Table 2 presents the misfit per data component; the RMS for the apparent resistivities of the TE mode was extremely low (<0.02 per cent not shown) as it is a result of the large error floor settings. For both profiles, the RMS of TMρ_a and TMϕ are close to the global average. Yet, RMS of TEϕ is considerably larger than the other transfer functions. Tight errors on the TMρ_a may have given more relevance to the fitting of the TM mode responses. More importantly, the TE mode is more sensitive to 3-D variations along strike and off-profile, and it is also known that the topographic effect is expressed as galvanic distortion (e.g. Jiracek 1990). Considering that the topography along the profile is included in the model but not across, and that strong 3-D effects were observed in the data set (see Section 3.2) superior fit of TM in comparison to TE mode data can be expected.

Fig. 11 provides a detailed analysis of the RMS values per station and period for the northern and southern sections colour-coded for each mode and response. In both cases (Figs 11a and b), the stations with the largest RMS, particularly for the phases of the TE-mode (orange), are located above the MA where the influence of topography and 3-D structures is largest (see Fig. 5). Therefore, the TE and TM misfits are similar in the (1-D–2-D) basins, whereas they disagree in the MA. Similarly, data misfits increase with the period as sounding range widens and the influence of off-profile structures increases.

Fig. 12 shows the MT responses for six selected sites (marked in red in Fig. 11), four are from the northern and two from the southern sections. These stations represent the data set at different locations and elevations (see yellow triangles in Fig. 10). Sites 0005 and 0014 are located in the MB; sites 0029, 0036 and 0042 in the MA; site 0057 is from the BAB.

Due to the tight error floor settings, the phases of both TM and TE mode are generally well fitted. Also, TM resistivities are well matched throughout the data set. TE apparent resistivity responses reproduce the shapes of the measured data, but may be shifted in parallel (e.g. 0042, 0036 and 0014 in Fig. 12). The results at these stations demonstrate that our chosen inversion setting can handle static shift in the TE mode apparent resistivity.

The stations above the MB (0005 and 0014) and BAB (0057) show responses in agreement with the 1-D/2-D dimensionality observed from the PT. The apparent resistivity and phase curves similarly show little variation for periods between 10^{-3} and 1 s. The split of TE and TM modes at longer periods is likely associated with a change from sedimentary rocks to bedrock formations.

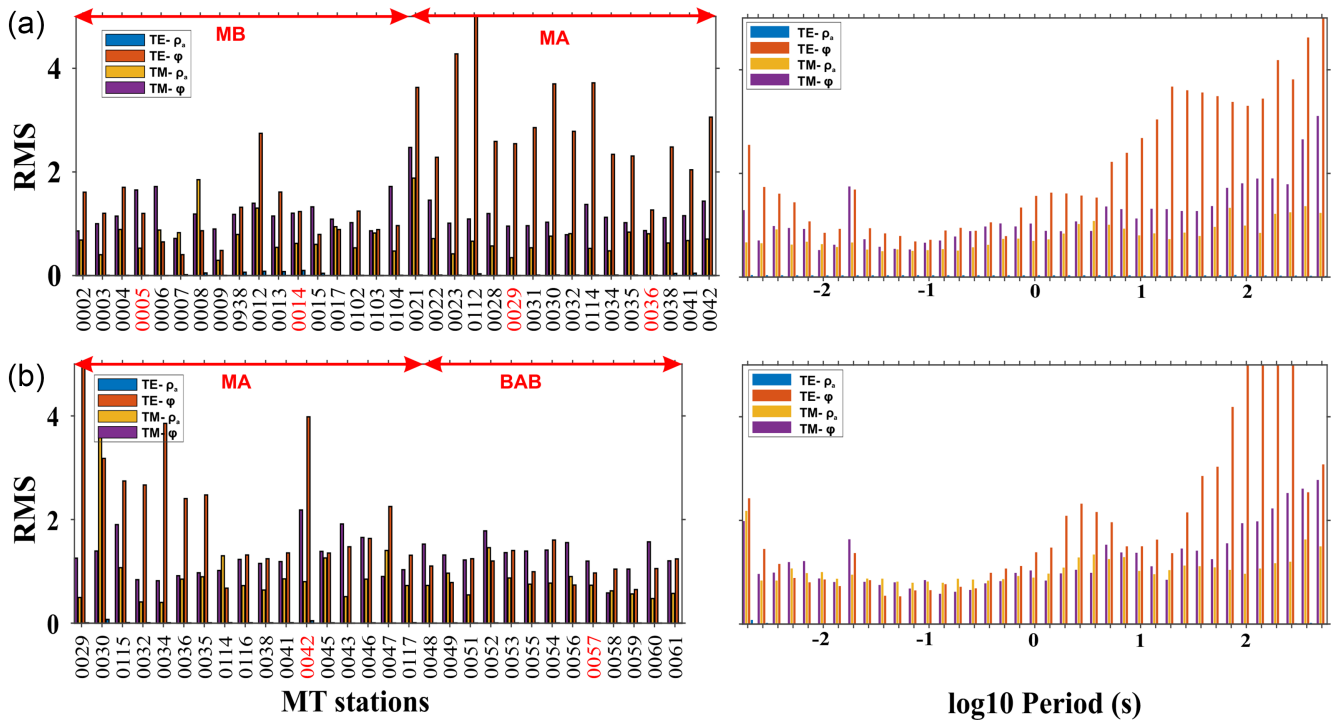

Figure 11. Misfit breakdown for (a) the northern and (b) southern sections, show the RMS per station (left-hand panel) and per period (right-hand panel). Stations labelled in red are shown in Fig. 12. The red arrows mark the surface extensions of the MB, MA and BAB.

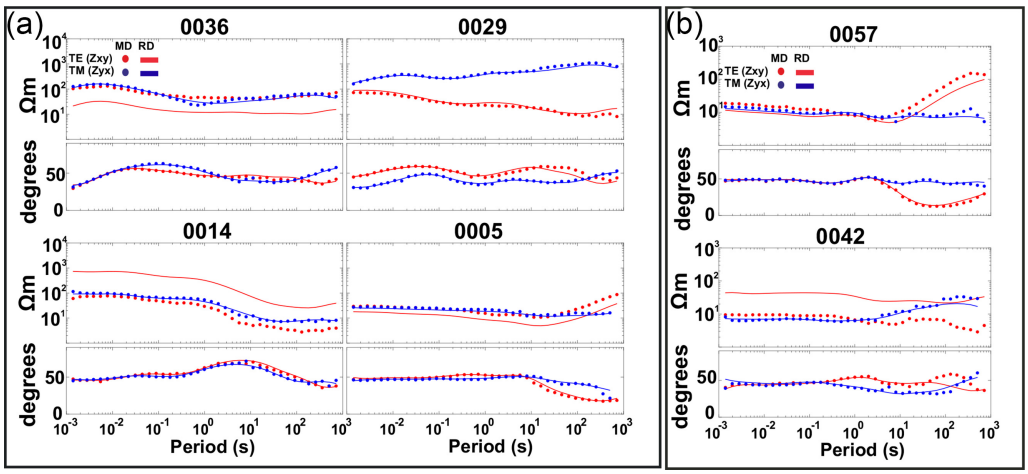

Figure 12. Responses of 2-D inversions for selected stations from (a) the northern section (sites 0036, 0029, 0014 and 0005) and (b) the southern section (sites 0057 and 0042). Dots represent measured data and lines show inversion results. Red and blue indicate TE and TM mode, respectively. Station locations are marked in Fig. 10 with yellow triangles.

Sites 0036 and 0029 are located in the central section and the PT analysis suggested strong 3-D effects and topographic variations (Fig. 3). Nevertheless, data at both stations are well fitted (Fig. 12a). A strong resistivity contrast nearby causes the splitting of TE and TM mode responses of station 0029.

5.3 Model sensitivity and resolution test

Model sensitivities are the partial derivatives of the electric and magnetic fields at each receiver with respect to the conductivity parameters of the inverse model. Analysis of the model sensitivities allows us to recognize whether a model parameter is sensitive to the data or not (Schwalenberg *et al.* 2002). Fig. 13 shows the normalized model sensitivities derived from the TE and TM modes and weighted by their respective grid sizes (Schwalenberg *et al.* 2002) for the 2-D inversions of northern and southern sections (Fig. 10).

To investigate which sections of the model influenced the responses the most, features labelled with C for conductors and R for resistors in the 2-D inversions of measured data (Fig. 10) were independently substituted by more resistive and more conductive bodies, respectively. Forward responses of these modified models were then calculated and new inversions started.

We found that structures located in areas with model sensitivities above $10^{-6.5}$, for the northern sections, and 10^{-6}, for the southern section (blue bars in Fig. 13), have a significantly higher influence on the forward responses of the models than the ones below this limits.

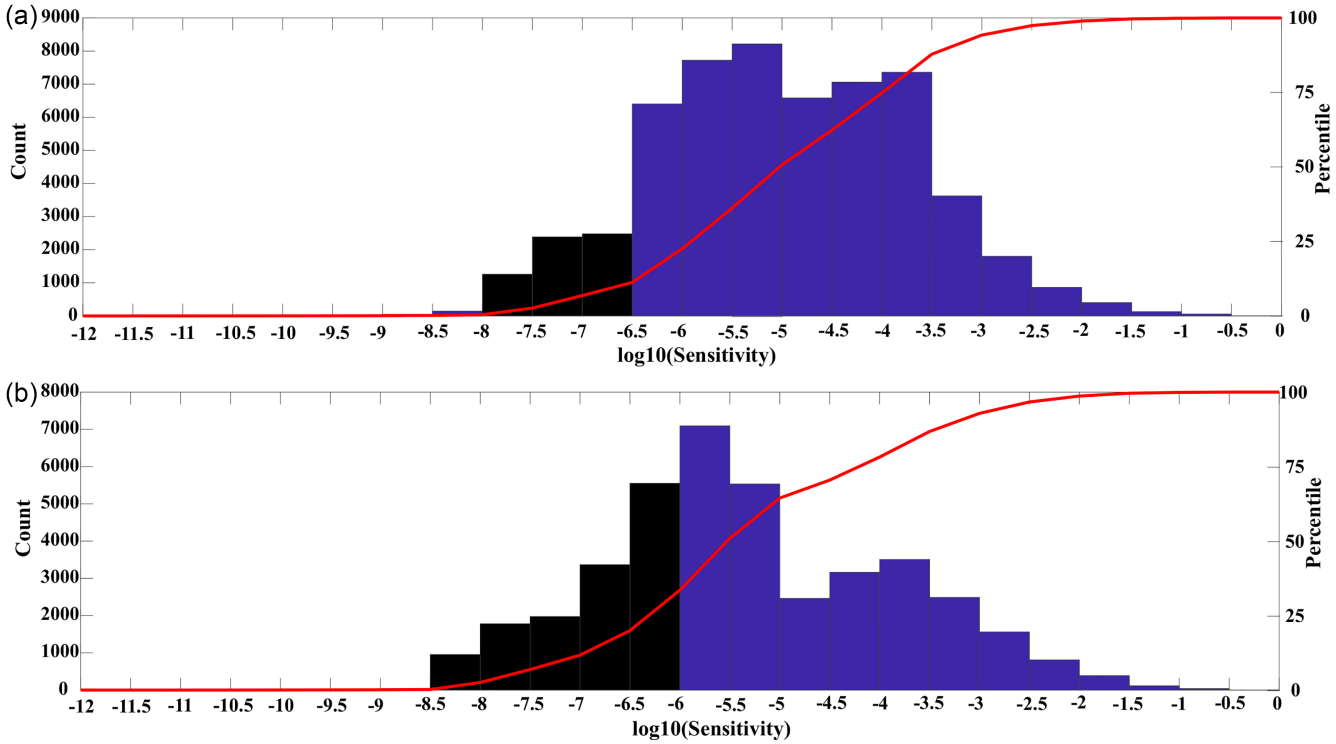

Figure 13. Bar chart and cumulative percentage of the model sensitivities of the grid elements of the 2-D inversion models presented in Fig. 10 for the (a) northern and (b) southern sections. The x-axis represent the model sensitivities weighted by the size of the grid elements in logarithmic scale. Blue bars represent those elements whose sensitivities are higher than $10^{-6.5}$ for A and 10^{-6} for B (see text for explanations).

Therefore, we restrict our interpretations to areas with sensitivities above this thresholds. Accounting for roughly 88 per cent of the grid elements of the 2-D inversion model in the northern section (Fig. 13a) and 67 per cent of the grid elements in the southern section (Fig. 13b). Regions with lower sensitivities are grey shaded in Figs 13(a) and (b).

Furthermore, the modified models show that misfits in the vicinity of the modified structures increased considerably. After rerunning the inversions the misfits returned to their previous levels and the substituted features reappeared roughly with the same extents, shapes, depths and resistivities. The recovery of these structures after inversion of the modified models strongly suggest that they are required features to explain the data.

5.4 Geological interpretation

The MB is mostly associated with the horizontally extended conductors C1 and C2 (Fig. 10a) and generally enhanced electrical conductivities surrounding them. Most specifically they could be related to the younger Tertiary sediments on top of the basin with depths ranging between 3 and 7 km, and resistivities between 1 and 5 Ωm. Depths of these conductors mirror the depths reported by Escalona & Mann (2003) for the eastern part of the basin. The deeper extension of C1 may be related to the BNF, a right-lateral strike-slip fault with an undetermined amount of horizontal offset (Escalona & Mann 2006a). C1 reaches a maximum depth in our inversion of approximately 9 km and resistivities between 1 and 50 Ωm.

Resistor R1 is located under stations with low β values and small IVs for short periods that are compatible with 1-D/2-D conditions (see Fig. 5a). According to Escalona & Mann (2003, 2006a), this area is characterized by a thick Eocene depocentre (∼5 km) with a high hydrocarbon content exposed by folding and faulting. Our models estimate depth for R1 of up to 10 km and resistivities between 100 and 1000 Ωm. We speculate that accumulated deformation related to the eastward movement of the North Andean Block may be responsible for the lateral variations of conductors and resistors (C1–C2–R1) in this area.

Conductors C3 and C4 reaching depths up to 12 km and resistivities between 1 and 7 Ωm. (Fig. 10a), could image the thrust front of the northern face of the MA (NWTS in Fig. 2) and the VF. C3 appears as a U-shaped structure similar to conductor C3 in Fig. 8(a). As discussed above, the MT responses of stations 0102, 0103 and 0104 east of the VF (see Fig. 3) are highly influenced by electric currents aligned with this fault system, which functions as a local conductive anomaly subparallel to the profile. This 3-D effect shapes conductor C3 in Fig. 10(a) and prevents it from correlating spatially with the fault planes. Resistor R2 (in Fig. 10a) could correspond to the Jurassic sediments of the La Quinta formation (Hackley *et al.* 2006), which are exposed at the surface. This structure seems to be limited by fault strands from the NWTS and VF with a maximum depth of 8 km and resistivity of 100 Ωm.

The MA generally appears as a resistive structure divided into northwards and southwards dipping flanks separated by a large conductor (C5 in Fig. 10a). The central part of the MA consists mostly of Cenozoic and Mesozoic igneo-metamorphic rocks (Yrigoyen & Urien 1988). Which explains the high resistivity near the surface of the Mérida Andes (> 500 Ωm), consistent with a pre-Palaeozoic basement of igneous and metamorphic rocks exposed at the surface (Fig. 2). Conductor C5 appears as two disconnected bodies one vertical and another one subhorizontal with resistivity values between 0.1 and 10 Ωm. We interpret C5 as the BF, with a maximum depth of about 12 km. For the first 7 km, the fault is vertical and then

inclined almost horizontally towards the SE. As the rotated profile is close to the original profile, the surface trace of the BF is not skewed much by projection errors.

The BAB appears to be mostly 1-D, based on the results from the dimensionality and directionality analysis. In Fig. 10(b), basin depths range between 2 and 5 km (conductors C8 and C9). These results are congruent with those reported from seismic data for the basin (Chacín *et al.* 2005). Resistivity values range between 2 and 20 Ωm, as can be expected for basins filled with unconsolidated Quaternary sediments and in contrast to the crystalline bedrock (Callejón & von der Dick 2002) (R4 $\rho > 500$ Ωm). C8 and C9 are separated by resistor R3 (Fig. 8b). Conspicuously, R3 appears at a location with poor site coverage and could be the result of poor resolution, an effect also observed in the synthetic data (*cf.* C9 Fig. 8b). The conductor C7 with a depth of 4 km may be associated with the Southeastern Thrust System (SETS) and Cenozoic sediments outcropping in this area. C6 may be the image of the BF but occurs with an offset due to the projection of the rotated profile. The black circle in Fig. 10(b) marks a conductive body at great depth similar to that seen in synthetic models (Fig. 8b). The synthetic modelling suggests that such structures are caused by off-profile features. Therefore this deep conductivity anomaly should be interpreted with caution.

Conductive anomalies modelled under the MA differ considerably between the northern and southern sections (Fig. 10). Our 2-D inversion test with synthetic data set suggest that 3-D structures can still be 2-D interpreted and that the differences between models are related to the projection of stations onto a profile and data rotation. Also showing that these effects are further exaggerated by larger distances in stations projections. Therefore the best model to address the structures under the MA and the observed 3-D effects is the northern section.

5.5 The effect of off-profile features in 2-D inversions of measured data

Off-profile structures can have a considerable effect in shaping the resulting structures of 2-D inversion models. The aforementioned U-shaped conductor C3 (Fig. 10a) is associated with the N–S trace of the VF east of the profile. The synthetic data showed that this oblique feature influences mostly on sites 0102, 0103 and 0104 (see Figs 3 and 9a). To study this effect further we repeated the inversion of the northern section excluding these stations. The resulting model (Fig. 14) converged after 39 iterations and reduced an initial RMS of 22.46 to 1.23 (TEφ: 1.99, TMρ_a: 0.75, TMφ: 1.14). The slight reduction in the RMS after the exclusion compared to the previous inversion (Table 2) suggest that the 3-D effect affected sites locally but had no major impact on the entire model.

The exclusion of sites 0102, 0103 and 0104 (Fig. 14) revealed a different shape of C3 and resulted in a more prominent resistor R2 in contact with the NWTS. Conductor C3 appears as a thin subvertical structure, reflecting our expectations of a fault separating the *MA* from the MB. The maximum depth of resistor R1 is now imaged at 9 km, still considerably deeper than the 5 km derived from seismic data (Escalona & Mann 2006a) for the Eocene sediments.

Excluding stations influenced by off-profile structures allows for better mapping of the MA's northern deformation front, represented by the northwestern thrust system and the VF. However, it could also lead to poorer site coverage above R2. As seen with synthetic data (i.e. C1-3 and C9 in Fig. 8) uneven spatial distribution of stations can cause placement of resistors in conductive areas, or exaggerate them.

Fig. 15 shows a comparison of the 2-D inversions of the entire profile rotated to –116° of the measured (A) the synthetic data (b) and the corresponding section of a synthetic 3-D model (c). The profile in Fig. 15 is an extension of the northern section towards the south, now including all the stations in the profile (see dotted line AA" in Fig. 3). The synthetic data were created using the simplistic 3-D model described in Section 4, which resembles the most prominent and well-known features in the area. The subsequent 2-D inversion of the 3-D data set resulted in complex conductivity anomalies, which in some cases seemed to have changed in shape or were skewed when projected onto the 2-D profile plane. A screening effect can occur if highly conductive structures at the surface reduce the penetration of the electromagnetic fields. The black rectangle (Fig. 15a and b) shows such a conductive structure smeared out to deeper levels and towards the southeast. Beneath the structure marked by the black rectangle, a homogeneous resistive body deepens southwards (at 60 km depth). However, this body appears where the model sensitivities are low ($<10^{-6}$). Despite its relatively large size, this resistor has practically no effect on fitting the southernmost stations; it could be a regularization artefact.

The conductive anomaly marked with the red ellipse in Fig. 15(b) could be a projection of the off-profile feature labelled with OPC in Fig. 15(c). Synthetic data generated with and without the OPC (not shown here) produce the conductive anomaly marked by the yellow circle Fig. 15(b). This anomaly is likely related to the oblique transition from background resistivity (500 Ωm) to the conductive BAB basin (25 Ωm). Similar effects are observed in Fig. 15(a), where the conductive feature highlighted by the red ellipse appears to be the projection of an off-profile feature, modelled in a zone with low sensitivities. The conductor marked by the yellow circle is then attributed to the obliquely striking contrast with the BAB.

Under the central section of the profile, a pronounced conductive anomaly appears, which is outlined by black ellipses in Figs 15(a) and (b). This conductive feature is a projection of the off-profile conductor to the northeast (OPC in Fig. 7). Its location was inferred from its significant influence on the direction and size of the observed IV (Figs 5a–c). The IV seem to locate the conductive anomaly to the northeast of the profile, but its exact position is poorly resolved as there is no station coverage. This conductivity zone at great depth (black ellipse in Fig. 15a) was observed in inversion models employing different approaches. We generated several synthetic data sets from 3-D models including a conductive structure to the east of the profile testing different conductivities for the structure, depths, thickness and extents, ultimately using different fault systems as limits for the structure. We also tested the 2-D inversions with different geoelectrical strikes, more conductive or resistive initial models and constrained inversion introducing resistivity boundaries at certain depths. Particularly by limiting the range of resistivity variations below 40 km and by fixing the resistivity, the models showed a thinner anomaly than the originally recovered similar in extension and conductivity, closely above the fixed zone. In the end, all of the inversion models showed a conductive block somewhere below the VF and the BF and undoubtedly such a feature is required to fit the data with 2-D inversion.

The sensitivity test showed that this structure influences approximately 30 sites (0014–0045) at long periods (>100 s). From the theory of MT, we know that the induction range widens with increasing period. This means that the conductive off-profile structure must be located at greater depth, at a lateral distance from the stations, or a combination of both. The location at a lateral distance is supported by the IV which clearly indicate a conductive feature

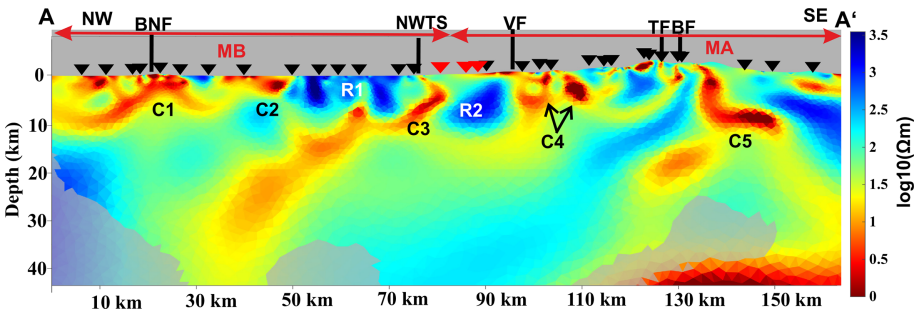

Figure 14. 2-D inversion results of the Northern section after excluding stations deemed influenced by an off-profile NS trace of the VF. Red triangles mark the excluded stations. Conductive and resistive structures are labelled as in Fig. 10(a). The grey shaded area represent sections of the model with sensitivities lower than $10^{-6.5}$. Surface locations of fault systems are indicated by black lines; the extents of the MA and MB are depicted by red arrows.

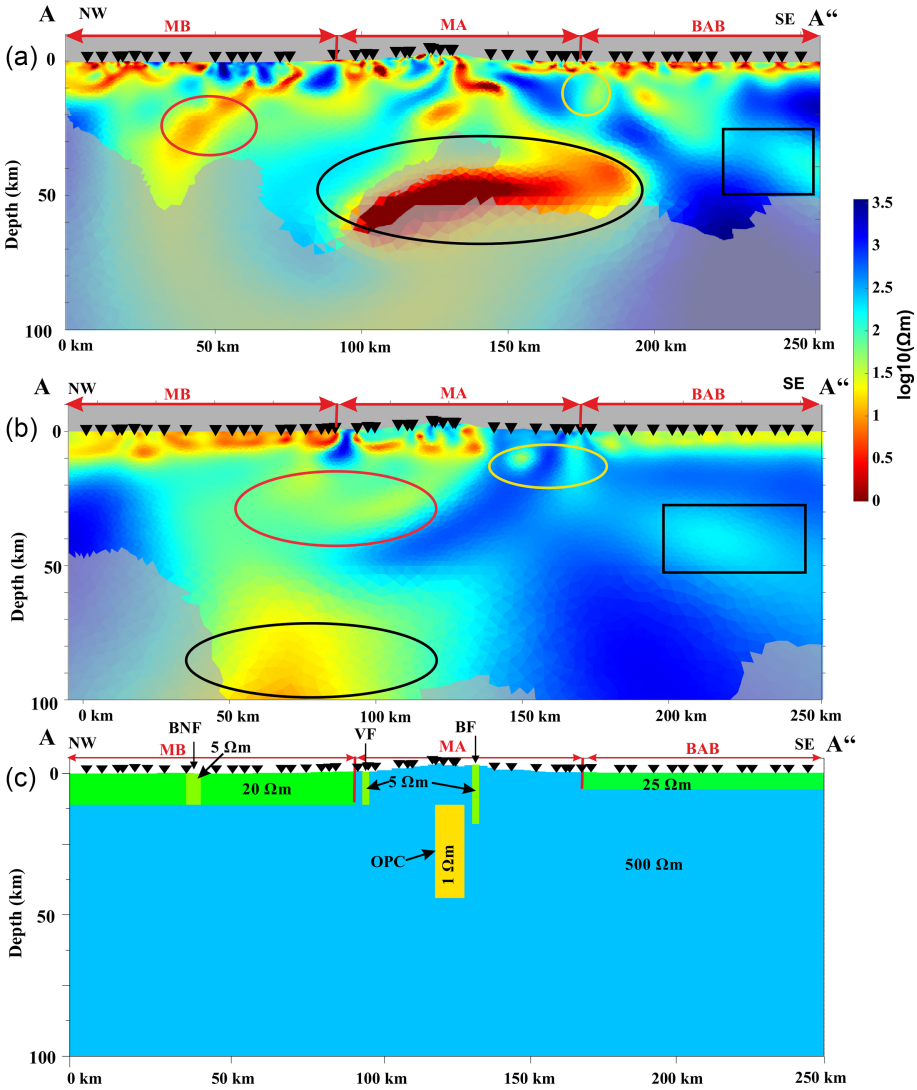

Figure 15. 2-D sections along a profile striking with a N26°E direction (dotted line AA" in Fig. 3) showing inversion results (rotated to –116°) for (a) the measured (b) synthetic data, and (c) a corresponding excerpt of the synthetic 3-D model. Areas marked by circles and rectangles are discussed in the text. The locations of the fault systems in the 3-D model are marked with black arrows (see also Fig. 7a). The conductor labelled OPC in C is an off-profile feature (see Fig. 9 for lateral extension). The grey shaded areas represent sections of the models with sensitivities lower than $10^{-6.5}$.

east of the profile particularly for periods larger than 10 s. Comparison of the 2-D inversion of measured data with the 3-D model showed that this off-profile anomaly could be associated with the NE displacement of the Trujillo Block. According to Dhont *et al.* (2012), this block is limited by the BF and the VF and has a detachment surface at about 15 km depth. The motion of the Trujillo block is accompanied with widespread extension towards the NE accommodated by normal faults (Dhont *et al.* 2012).

High conductivity crustal anomalies are often associated with the presence of fluids. The detachment of the Trujillo block could provide a pathway for fluids, which may originate from re-mineralization processes associated with the subduction of the Caribbean plate. Deep reaching fault systems of the area (e.g. the VF and the BF) may even provide pathways for such fluids towards the surface.

6 DISCUSSION AND CONCLUSIONS

The MT profile acquired across the MA, from the central part of the BAB and into the MB basins, resulted in a first image of the deep electrical conductivity structure of the subsurface of western Venezuela. The dimensionality and directionality analyses of the MT data suggested that the northern and southern parts of the data set are generally consistent with 1-D/2-D assumptions, but also that the MA section is strongly effected by 3-D structures. It was, therefore, essential to investigate and quantify how 3-D effects affect the outcome of 2-D inversion, the tool commonly used for data acquired along a profile.

To solve the 2-D inverse problem, we used the finite elements (FE) code MARE2DEM (Key & Ovall 2011; Key 2016). We put a strong emphasis on fitting the phases of the TE- and TM-modes with the 2-D inversions, as they are not affected by galvanic distortion. The apparent resistivities, particularly for the TE mode, were downweighted. Similar approaches were used by other authors in similarly complex topographic and geological settings (e.g. Meqbel 2009; Sass *et al.* 2014; Muñoz *et al.* 2018). The IV are generally small and poorly resolved for the basin areas. They became larger in the central MA section but pointing in varying directions. All attempts to include them in the 2-D inversions failed. We tested other inversion parameters intensively, including values for background resistivity, grid sizes, detail of topography, the inclusion of the Caribbean Sea to account for the coast effect, regularization and the trade-off parameter that weights regularization against data fit.

As expected, the 2-D inversion of the field data could recover the BAB and MB sedimentary basins (Figs 10b and 14). The depths of the basins (5 km for the BAB and 7 km for the MB) are consistent with results from seismic studies (Callejón & von der Dick 2002; Chacín *et al.* 2005; Escalona & Mann 2006a, b). Sensitivity tests confirmed that resistivity, extent and shape of the structures are robust. The lateral transition of conductors and resistors in the northern section (C1, C2 and R1 in Fig. 14) could be related to deformation (folding of sedimentary sequences) caused by the eastward movement of the North Andean Block (NAB).

A major finding of our 2-D inversions was a conductive zone at great depth (black ellipse in Fig. 15). With our conceptual 3-D models, we could demonstrate, however, that this feature was caused by the projection of an off-profile conductor to the east. We used ModEM (Meqbel 2009; Egbert & Kelbert 2012) for the 3-D modelling. The conceptual 3-D models contained simplified regional geological and tectonic structures (Figs 1 and 2), including all major regional sedimentary basins, the Caribbean Sea, major fault systems, and eventually a significant off-profile conductor associated with the Trujillo Block (see Fig. 9). The location of the Trujillo Block east of the profile was inferred from the observed IV (Figs 5a–c) but its exact position is poorly resolved as there is no station coverage. From these 3-D models, we generated synthetic data with the same station distribution as the measured data. 2-D inversions of the synthetic data confirmed that the off-profile conductor appears as a spurious feature at depth in the 2-D sections.

We tested other marked features appearing in the 2-D inversion images with this method and found that obliquely striking fault systems can also appear as artefacts or strongly distorted (e.g. C4, C5 and C6 in Fig. 8). Horizontally elongated structures crossing the profile obliquely can generally appear with a vertical and/or horizontal offset in the 2-D sections. We also found that the uneven station coverage combined with the regularization (smoothing) used in our 2-D inversions foster the inclusion of separate bodies within originally contiguous layers (e.g. C9 in Fig. 8). To reproduce the lateral extension of these structures 2-D inversion tends to overestimate their conductivity, partially explaining the generally low resistivity values of the fault systems in our 2-D inversions. Our results clearly emphasize the importance of off-profile structures on MT data, particularly when 2-D interpretation tools are used.

The central part of the MA consists of Cenozoic and Mesozoic igneo-metamorphic rocks, which appear generally as resistive material. Zones of high conductivity in the MA often correlate with major fault systems. Particularly, the BF correlates with C5 (see Fig. 14), forming a subvertical fault plane that changes its direction from vertical to subhorizontal at approximately 12 km depth, which may represent a detachment plane at mid-crustal levels, consistent with existing geodynamic models (e.g. Audemard & Audemard 2002; Duerto *et al.* 2006; Monod *et al.* 2010; Dhont *et al.* 2012).

Our study shows that it is at least reasonable to link the associated off-profile conductivity anomaly with the Trujillo Block, more specifically with a detachment surface resulting from the northeastward tectonic escape of this block. The Trujillo block is bounded laterally by both the BF and Valera fault (VF) systems and is assumed to have a detachment level at mid-crustal depth (15 km, Dhont *et al.* 2012). This block plays a key role in recent geodynamic models developed for northwestern Venezuela (e.g. Audemard & Audemard 2002; Monod *et al.* 2010), as it could be absorbing one quarter of the deformation related to the oblique converge in the MA (e.g. Dhont *et al.* 2005; Backé *et al.* 2006; Monod *et al.* 2010). High conductivities in active tectonic zones have often been associated with fluids and hydrous minerals (e.g. Ritter *et al.* 2005; Unsworth 2009; Meqbel *et al.* 2014). The low resistivity associated with the Trujillo Block could originate from mineralized shear planes or from fluids, possibly arising from the subduction of the Caribbean plate. But more MT data with a much better aerial coverage and 3-D inversions would be required to confirm this speculation.

Much better resolved are the zones of high conductivity associated with the fault systems of the MA. The most prominent tectonic features of the MA are the 500-km-long BF and the 240-km-long left-lateral strike-slip VF. These fault systems may provide pathways for meteoric water or fluids generated at depth. Drainage and alluvial deposits are reported along the strike of the BF (Audemard & Audemard 2002). Clay minerals in fault gauges may also contribute to the high conductivity of the strike-slip faults (Unsworth *et al.* 1997).

The current settings of western Venezuela can be described by floating blocks or orogens, whose current deformations are controlled by the relative movement of the Caribbean and South American plates. Monod *et al.* (2010), present an orogenic float model for the MA based on the orogenic float concept for transpressional orogens (Oldow *et al.* 1990). In this model, the BF is considered an upper crustal fault that connects to a mid-crustal detachment level, which allows the orogen to float within the lithosphere. Balanced sections crossing the MA suggest 40 km of shortening in the southern part of the belt and 30 km in the northern part. Moreover, based on shear wave splitting analysis, Masy *et al.* (2011) propose the BF to cause deformation at lithospheric scale.

The electrical structures revealed by our study agree in general with the floating blocks model and geodynamic processes dominated by the northeastwards escape of the North Andean Block and its interaction with the Caribbean and South American plates.

ACKNOWLEDGEMENTS

The study was performed within the scope of the Integrated Geosciences of the Mérida Andes project (GIAME) funded by FONACIT 012002202 and Petróleos de Venezuela, S.A. (PDVSA)12.09.2012 grants, with support from GFZ Potsdam (GFZ-FUNVISIS cooperation agreement from 11/12/2014). The equipment for the field work was supplied by the Geophysical Instrument Pool Potsdam (GIPP) of the GFZ Potsdam. JC gratefully acknowledges financial support from the German Academic Exchange Service (DAAD, German acronym) and continuing support from the GFZ Potsdam and FUNVISIS. This project required intensive field work which would have not been possible without the effort from researchers and students of FUNVISIS, GFZ-Potsdam, PDVSA, PDVSA-INTEVEP, Venezuelan Central University (UCV) and Simón Bolívar University (USB) which we gratefully acknowledge. We also wish to acknowledge the support from land owners for allowing installation on their properties. JC express gratitude towards the two anonymous reviewers whose insightful comments improve considerably the clarity of this paper.

REFERENCES

Amante, C. & Eakins, B.W., 2009. ETOPO1 1 arc-minute global relief model: procedures, data sources and analysis, Tech. rep., NOAA Technical Memorandum NESDIS NGDC-24.

Arnaiz-Rodríguez, M.S., Rodríguez-Millán, I. & Audemard, F., 2011. Análisis gravimétrico y flexural del occidente de Venezuela, *Revista mexicana de ciencias geológicas,* **28,** 420–438.

Audemard, F.A., 1999. Morpho-structural expression of active thrust fault systems in humid tropical foothills of Colombia and Venezuela, *Zeit. Geomorphol.,* **118**(1), 1–18.

Audemard, F.A., 2003. Geomorphic and geologic evidence of ongoing uplift and deformation in the Mérida Andes, Venezuela, *Quater. Int.,* **101-102**(1), 43–65.

Audemard, F.A., 2014, Active block tectonics in and around the Caribbean: a review, in *El Límite Noreste de la Placa Suramericana - Estructuras Litosféricas de la Superficie al Manto (The Northeastern Limit of the South American Plate - Lithospheric Structures from Surface to the Mantle),* 1st edn, Chapter 2, pp. 29–77, eds Schmitz, M., Audemard, F. & Urbani, F., Editorial Innovación Tecnológica, Facultad de Ingeniería-Universidad Central de Venezuela/FUNVISIS.

Audemard, F.A., Machette, M.N., Cox, J.W., Dart, R.L. & Haller, K.M., 2000. Map and database of Quaternary faults in Venezuela and its offshore regions, Tech. rep., US Geological Survey.

Audemard, F.A., Singer, P.A., Soulas, J.P. & FUNVISIS Earth Sciences Deparment, N.S., 2006. Quaternary faults and stress regime of Venezuela, *Rev. Asoc. Geol. Argent.,* **61**(4), 480–491.

Audemard, F.E. & Audemard, F.A., 2002. Structure of the Mérida Andes, Venezuela: relations with the South America–Caribbean geodynamic interaction, *Tectonophysics,* **345**(1–4), 1–26.

Backé, G., Dhont, D. & Hervouët, Y., 2006. Spatial and temporal relationships between compression, strike-slip and extension in the Central Venezuelan Andes: Clues for Plio-Quaternary tectonic escape, *Tectonophysics,* **425**(1–4), 25–53.

Bahr, K., 1988. Interpretadon of the magnetotelluric impedance tensor: regional induction and local telluric distortion, *J. Geophys.,* **62,** 119–127.

Becken, M. & Burkhardt, H., 2004. An ellipticity criterion in magnetotelluric tensor analysis, *J. geophys. Int.,* **159**(1), 69–82.

Becken, M. & Ritter, O., 2011. Magnetotelluric studies at the San Andreas fault zone: implications for the role of fluids, *Surv. Geophys.,* **33**(1), 65–105.

Becken, M., Ritter, O. & Burkhardt, H., 2008. Mode separation of magnetotelluric responses in three-dimensional environments, *J. geophys. Int.,* **172**(1), 67–86 .

Becken, M., Ritter, O., Bedrosian, P.A. & Weckmann, U., 2011. Correlation between deep fluids, tremor and creep along the central San Andreas fault, *Nature,* **480**(7375), 87–90.

Bibby, H.M., 1986. Analysis of multiple-source bipole-quadripole resistivity surveys using the apparent resistivity tensor, *Geophysics,* **51**(4), 972–983.

Boerner, D.E., Craven, J.A., Kurtz, R.D., Ross, G.M. & Jones, F.W., 1998. The great falls tectonic zone: suture or intracontinental shear zone?, *Can. J. Earth Sci.,* **35**(2), 175–183.

Booker, J.R., 2013. The magnetotelluric phase tensor: a critical review, *Surv. Geophys.,* **35**(1), 7–40.

Brasse, H., 2011. Electromagnetic images of the South and Central American Subduction Zones, in *The Earth's Magnetic Interior, Vol. 1 of IAGA Special Sopron Book Series,* pp. 43–81, eds Petrovský, E., Ivers, D., Harinarayana, T. & Herrero-Bervera, E., Springer.

Cagniard, L., 1953. Basic theory of the magnetotelluric method of geophysical prospecting, *Geophysics,* **1**(18), 605–635.

Caldwell, T.G., Bibby, H.M. & Brown, C., 2004. The magnetotelluric phase tensor, *J. geophys. Int.,* **158**(2), 457–469.

Callejón, A.F. & von der Dick, H.H., 2002. Numerical identification of microseeps in surface soil gases of western Venezuela, and its significance for hydrocarbon exploration, in Surface exploration case histories: publications of geochemistry, magnetics, and remote sensing, *AAPG Stud. Geol. and SEG Geophysical References Series,* **11**(48), 381–392.

Chacín, L., Jácome, M.I. & Izarra, C., 2005. Flexural and gravity modelling of the MéRida Andes and Barinas–Apure Basin, Western Venezuela, *Tectonophysics,* **405**(1–4), 155–167 .

Constable, S.C., Parker, R.L. & Constable, C.G., 1987. Occam's inversion: a practical algorithm for generating smooth models from electromagnetic sounding data, *Geophysics,* **52**(3), 289–300.

De Toni, B. & Kellogg, J., 1993. Seismic evidence for blind thrusting of the northwestern flank of the Venezuelan Andes, *Tectonics,* **12**(6), 1393–1409.

Dewey, J.W., 1972. Seismicity and tectonics of western Venezuela, *Bull. seism. Soc. Am.,* **62**(6), 1711–1751.

Dhont, D., Backé, G. & Hervouët, Y., 2005. Plio-quaternary extension in the Venezuelan Andes: mapping from sar jers imagery, *Tectonophysics,* **399**(1–4), 293–312.

Dhont, D., Monod, B., Hervouët, Y., Backé, G., Klarica, S. & Choy, J.E., 2012. 3D geological modeling of the Trujillo Block: insights for crustal escape models of the Venezuelan Andes, *J. South Am. Earth Sci.,* **39,** 245–251.

Duerto, L., Escalona, A. & Mann, P., 2006. Deep structure of the MéRida Andes and Sierra de Perijá Mountain fronts, Maracaibo Basin, Venezuela, *AAPG Bull.,* **90**(4), 505–528.

Egbert, G.D. & Kelbert, A., 2012. Computational recipes for electromagnetic inverse problems, *J. geophys. Int.,* **189,** 251–267.

Escalona, A. & Mann, P., 2003. Three-dimensional structural architecture and evolution of the eocene pull-apart basin, central Maracaibo Basin, Venezuela, *Mar. Petrol. Geol.,* **20**(2), 141–161.

Escalona, A. & Mann, P., 2006a. Tectonic controls of the right-lateral burro negro tear fault on paleogene structure and stratigraphy, northeastern Maracaibo Basin, *AAPG Bull.,* **90**(4), 479–504.

Escalona, A. & Mann, P., 2006b. An overview of the petroleum system of Maracaibo Basin, *AAPG Bull.,* **90**(4), 657–678.

Forbes, J.M., 1981. The equatorial electrojet, *Rev. Geophys.,* **19**(3), 469–504.

Gamble, T.D., Goubau, W.M. & Clarke, J., 1979. Magnetotellurics with a remote magnetic reference, *Geophysics,* **44**(1), 53–68.

Garcia, R. & Campos, C., 1977. Evolucion tectonica e historia geologica de la region de Valera-Escuqeu, Estados Trujillo y Zulia, in *II Cong.*

Latino-Americano Geol., Caracas (1973), no. 1 in 3, pp. 1825–1836, Bol. Geol. Publ. Espec.

García Juanatey, M., Hübert, J., Tryggvason, A. & Pedersen, L.B., 2012. Imaging the Kristineberg mining area with two perpendicular magnetotelluric profiles in the Skellefte Ore district, northern Sweden, *Geophys. Prospect.,* **61**(1), 200–219.

González de Juana, C., Iturralde, J.M. & Picard, X., 1980. *Geología de Venezuela y sus cuencas petrolíferas,* 1–2, Ediciones Foninves.

Hackley, P.C., Urbani, F., Karlsen, A. & Garrity, C., 2006. Geological shaded relief map of Venezuela, Tech. rep., U.S. Geological Survey, Sheet 1 of 2.

Hanstein, T., Eilenz, E. & Strack, K.M., 1986. Einige aspekte der aufbereitung von lotem daten, in *EMTF colloquium*.

Hauff, F., Hoernle, K., Tilton, G., Graham, D. & Kerr, A.C., 2000. Large volume recycling of oceanic lithosphere over short time scales: geochemical constraints from the Caribbean large igneous province, *Earth planet. Sci. Lett.,* **174**(3–4), 247–263.

James, K.H., Lorente, M.A. & Pindell, J.L., 2009. *The Origin and Evolution of the Caribbean Plate, vol. 328 of 1,* Geological Society of London.

Jiracek, G.R., 1990. Near-surface and topographic distortions in electromagnetic induction, *Surv. Geophys.,* **11**(2-3), 163–203.

Jones, A.G., 1993. Electromagnetic images of modern and ancient subduction zones, *Tectonophysics,* **219**(1–3), 29–45.

Jones, A.G., Ledo, J. & Ferguson, I.J., 2005. Electromagnetic images of the Trans-Hudson orogen: the North American Central Plains anomaly revealed, *Can. J. Earth Sci.,* **42**(4), 457–478.

Kellogg, J. & Bonini, W., 1982. Subduction of the Caribbean Plate and basement uplifts in the overriding South American Plate, *Tectonics,* **1**(3), 251–276.

Kerher, L., 1925. Geological exploration of the Northern Trujillo mountains range foothills in the southern corner of Maracaibo basin, Tech. rep., Maraven.

Key, K., 2016. MARE2DEM: a 2-D inversion code for controlled-source electromagnetic and magnetotelluric data, *J. geophys. Int.,* **207**(1), 571–588.

Key, K. & Ovall, J., 2011. A parallel goal-oriented adaptive finite element method for 2.5-d electromagnetic modelling, *J. geophys. Int.,* **186**(1), 137–154.

Krings, T., 2007, The influence of robust statistics, remote reference, and horizontal magnetic transfer functions on data processing in magnetotellurics. *Master's thesis,* Institut fur Geophysik Westfalische Wilhelms-Universitat Munster and GeoForschungsZentrum Potsdam.

Kütter, S., Weckmann, U. & de Wit, M.J., 2016. A deep electrical conductivity structure of the southern Barberton Greenstone Belt, South Africa, derived from magnetotelluric measurements, *S. Afr. J. Geol.,* **119**(1), 273–290.

La Marca, E., 1997. *Origen y evolución geológica de la Cordillera de Mérida (Andes de Venezuela),* Facultad de Ciencias Forestales y Ambientales, ULA.

Ledo, J., 2005. 2-D versus 3-D magnetotelluric data interpretation, *Surv. Geophys.,* **26**(5), 511–543.

Masy, J., Niu, F., Levander, A. & Schmitz, M., 2011. Mantle flow beneath northwestern Venezuela: seismic evidence for a deep origin of the Mérida Andes, *Earth planet. Sci. Lett.,* **305**(3–4), 396–404.

Meqbel, N., 2009, The electrical conductivity structure of the Dead Sea Basin derived from 2D and 3D inversion of magnetotelluric data. *PhD thesis,* Free University Berlin.

Meqbel, N., Weckmann, U., Muñoz, G. & Ritter, O., 2016. Crustal metamorphic fluid flux beneath the Dead Sea Basin: constraints from 2-D and 3-D magnetotelluric modelling, *J. geophys. Int.,* **207**(3), 1609–1629.

Meqbel, N.M., Egbert, G.D., Wannamaker, P.E., Kelbert, A. & Schultz, A., 2014. Deep electrical resistivity structure of the northwestern U.S. derived from 3-D inversion of USArray magnetotelluric data, *Earth planet. Sci. Lett.,* **402,** 290–304.

Monod, B., Dhont, D. & Hervouët, Y., 2010. Orogenic float of the venezuelan andes, *Tectonophysics,* **490**(1–2), 123–135.

Mora, J.A., Oncken, O., Le Breton, E., Ibánez-Mejia, M., Faccenna, C., Veloza, G., Vélez, V., de Freitas, M. & Mesa, A., 2017. Linking Late Cretaceous to Eocene Tectonostratigraphy of the San Jacinto Fold Belt of NW Colombia with Caribbean plateau collision and flat subduction, *Tectonics,* **36**(11), 2599–2629.

Muñoz, G., Weckmann, U., Pek, J., Kováčiková, S. & Klanica, R., 2018. Regional two-dimensional magnetotelluric profile in West Bohemia/Vogtland reveals deep conductive channel into the earthquake swarm region, *Tectonophysics,* **727,** 1–11.

Oldow, J., Bally, A. & Avé Lallemant, H., 1990. Transpression, orogenic float, and lithospheric balance, *Geology,* **18**(10), 991.

Parkinson, W.D., 1959. Directions of rapid geomagnetic fluctuations, *Geophys. J.R. Astr. Soc.,* **2**(1), 1–14.

Pérez, O.J., Wesnousky, S.G., De La Rosa, R., Márquez, J., Uzcátegui, R., Quintero, C., Liberal, L., Mora-Páez, H. & Szeliga, W., 2018. On the interaction of the North Andes plate with the Caribbean and South American plates in northwestern South America from GPS geodesy and seismic data, *J. geophys. Int.,* **214**(3), 1986–2001.

Pindell, J., Kennan, L., Maresch, W.V., Stanek, K., Draper, G. & Higgs, R., 2005. Plate-kinematics and crustal dynamics of circum-Caribbean arc-continent interactions: tectonic controls on basin development in Proto-Caribbean margins, *Geol. Soc. Am., Spec. Paper.,* **394,** 7–52.

Platz, A. & Weckmann, U., 2019. An automated new pre-selection tool for noisy Magnetotelluric data using the Mahalanobis distance and magnetic field constraints, *J. geophys. Int.,* **218,** (3), 1853–1872.

Reddy, C.A., 1989. The equatorial electrojet, *Pure appl. Geophys.,* **131**(3), 485–508.

Ritter, O., Junge, A. & Dawes, G., 1998. New equipment and processing for magnetotelluric remote reference observations, *J. geophys. Int.,* **132**(3), 535–548.

Ritter, O., Hoffmann-Rothe, A., Bedrosian, P.A., Weckmann, U. & Haak, V., 2005. Electrical conductivity images of active and fossil fault zones, *Geol. Soc., Lond., Spec. Publ.,* **245**(1), 165–186.

Sass, P., Ritter, O., Ratschbacher, L., Tympel, J., Matiukov, V.E., Rybin, A.K. & Batalev, V.Y., 2014. Resistivity structure underneath the Pamir and Southern Tian Shan, *J. geophys. Int.,* **198**(1), 564–579.

Schubert, C. & Vivas, L., 1993. *El cuaternario de la Cordillera de Merida, Andes Venezolanos,* Fundacion Polar, Universidad Los Andes.

Schwalenberg, K., Rath, V. & Haak, V., 2002. Sensitivity studies applied to a two-dimensional resistivity model from the Central Andes, *J. geophys. Int.,* **150**(3), 673–686.

Soulas, J.P., Rojas, C. & Schubert, Y.C., 1985. Excursion no. 4, Neotectonica de las fallas de Bocono, Valera. Tuname y Mene Grande, in *VI Congresso Venezolano,* pp. 6961–6999.

Telford, W.M., Geldart, L.P., Sheriff, R.E. & Keys, D.A., 1977. *Applied Geophysics,* Cambridge Univ. Press.

Tietze, K. & Ritter, O., 2013. Three-dimensional magnetotelluric inversion in practice—the electrical conductivity structure of the san andreas fault in central california, *J. geophys. Int.,* **195**(1), 130–147.

Tikhonov, A.N., 1950. On determining electrical characteristics of the deep layers of the Earth's crust, *Dokl. Akad. Nauk. SSSR,* **1**(73), 295–297.

Unsworth, M., 2009. Magnetotelluric studies of active continent–continent collisions, *Surv. Geophys.,* **31**(2), 137–161.

Unsworth, M. & Bedrosian, P.A., 2004. On the geoelectric structure of major strike-slip faults and shear zones, *Earth, Planets Space,* **56**(12), 1177–1184.

Unsworth, M., Malin, P., Egbert, G.D. & Booker, J.R., 1997. Internal structure of the san andreas fault at parkfield, california, *Geology,* **25**(4), 359.

Urbani, F., 2017. *Distribución de los terrenos geológicos del Sistema Montañoso del Caribe, norte de Venezuela: Síntesis actualizada,* Boletín de la Academia Nacional de Ciencias Físicas, Matemíticas y Naturales.

Vozoff, K., 1991. *The Magnetotelluric Method,* Chapter 8, pp. 641–712, Society of Exploration Geophysicists.

Wannamaker, P.E., Hohmann, G.W. & Ward, S.H., 1984. Magnetotelluric responses of three-dimensional bodies in layered earths, *Geophysics,* **49**(9), 1517–1533.

Wannamaker, P.E., Stodt, J.A. & Rijo, L., 1986. Two-dimensional topographic responses in magnetotellurics modeled using finite elements, *Geophysics,* **51**(11), 2131–2144.

Weaver, J.T., 1994. *Mathematical Methods for Geoelectrical Induction,* Wiley.

Weckmann, U., Magunia, A. & Ritter, O., 2005. Effective noise separation for magnetotelluric single site data processing using a frequency domain selection scheme, *J. geophys. Int.,* **161**(3), 635–652.

Wiese, H., 1962. Geomagnetische tiefentellurik teil ii: Die streichrichtung der untergrundstrukturen des elektrischen widerstandes, erschlossen aus geomagnetischen variationen, *Geofisica Pura e Applicata,* **52**(1), 83–103.

Yrigoyen, M. & Urien, C.M., 1988. Cuadro Geostructural de la América del Sur, in *Geología de la América del Sur,* **Vol. 1,** pp. 17–106, Univ. Nac. Tucumán, Argentina.